Tracking the phase changes in micelle-based NiGa nanocatalysts for methanol synthesis under activation and working conditions

Uta Hejral[1], Janis Timoshenko[1], David Kordus[1,2], Mauricio Lopez Luna[1], Nuria J. Divins[2,¶], Simon Widrinna[1,2], Ioannis Zegkinoglou[2], Lukas Pielsticker[2,§], Hemma Mistry[2], Jorge Anibal Boscoboinik[3], Stefanie Kuehl[1], and Beatriz Roldan Cuenya[1*]

[1]*Department of Interface Science, Fritz-Haber Institute of the Max Planck Society, Berlin, Germany*
[2]*Department of Physics, Ruhr-University Bochum, 44780 Bochum, Germany*
[3]*Center for Functional Nanomaterials, Brookhaven National Laboratory, Upton, New York, USA*
[¶]*Present address: Institute of Energy Technologies, Universitat Politècnica de Catalunya, EEBE, Barcelona, Spain*
[§]*Present address: Department of Heterogeneous Reactions, Max Planck Institute for Energy Conversion, Mülheim an der Ruhr, Germany*
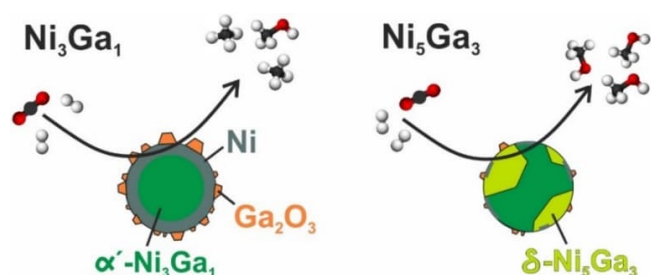
[*]e-mail: roldan@fhi-berlin.mpg.de

Abstract

The hydrogenation of CO_2 into high energy density fuels such as methanol, where the required H_2 is obtained from renewable sources, is of utmost importance for a sustainable society. In recent years, NiGa alloys have attracted attention as promising catalyst material systems for the hydrogenation of CO_2 into methanol at ambient pressures. They thus represent an energy-saving alternative to the Cu-based catalysts employed in today's catalytic industry that require high pressures for the CO_2 hydrogenation. However, the underlying reaction mechanisms for the NiGa system are still under debate. One of the challenges here is to unravel the evolution and coexistence of the different species in the heterogeneous NiGa catalyst system under activation and reaction conditions. To shed light on their evolution under H_2 activation and their catalytic roles under CO_2 hydrogenation working conditions on defined Ni_3Ga_1 and Ni_5Ga_3 nanoparticle (NP) catalysts, we employed a multi-probe approach. It included advanced machine learning-based analysis of *operando* X-ray absorption spectroscopy data combined with *operando* powder X-ray diffraction

and near ambient pressure X-ray photoelectron spectroscopy measurements, as well as reactivity studies using bed-packed mass flow reactors. In addition, we employed atomic force microscopy and scanning transmission electron microscopy for structural characterization.

Under H_2 activation at 1 bar total pressure, we conclude the formation of metallic Ni, starting for Ni_3Ga_1 at 300˚C, and for Ni_5Ga_3 at 400˚C. At higher temperatures, the formation of NiGa alloys follows. The α'-Ni_3Ga_1 alloy phase is predominantly formed for the Ni_3Ga_1 NPs, while the coexistence of α'-Ni_3Ga_1, δ-Ni_5Ga_3 and Ga_2O_3 phases is observed for the Ni_5Ga_3 NPs after the H_2 activation. The formation of the Ga_2O_3 phase also results in the presence of excess metallic Ni. Under CO_2 hydrogenation reaction conditions, Ga partially oxidizes again to form a Ga_2O_3-rich particle shell for both NP compositions, yet, to a larger extent for the Ni_3Ga_1 NPs, which, in turn, feature a higher amount of excess Ni. We reveal that metallic Ni is responsible for the high selectivity of the Ni_3Ga_1 NPs towards the production of methane in our catalytic tests. Contrary, the Ni_5Ga_3 NPs display a strong selectivity toward methanol production (>92%), more than one order of magnitude higher than that for the Ni_3Ga_1 NPs, which we ascribe to the presence of the δ-Ni_5Ga_3 phase.

GRAPHICAL ABSTRACT

1 Introduction

Against the background of dwindling resources for fossil fuels and the threats of climate change, sustainable and environmentally friendly production processes for fuels and chemical feedstocks become all the more important. Methanol, a liquid fuel of high energy density, may pave the way to such a desired sustainable society [1]. It can be produced from i) H_2 gained by electrochemical water-splitting using solar or wind power, and ii) the greenhouse gas CO_2,

extracted from air [2,3]. In contrast to using H_2 directly as a fuel, an infrastructure of ships, trucks and gas stations capable of handling the liquid fuel methanol already exists, which makes methanol a feasible alternative to fossil fuels in a shorter term. Moreover, methanol constitutes also one of the building blocks for a wide variety of synthetic materials [4], thus the annual demand for methanol keeps steadily growing.

In today's catalytic industry the synthesis of methanol is carried out from a gas mixture of H_2, CO and CO_2 over $Cu/ZnO/Al_2O_3$ catalysts, where high pressures (50 -100 bar) are required [5]. This traditional high pressure methanol synthesis does not only bring along safety risks and a high energy consumption, but restricts the CO_2 concentration to a maximum of about 10% of the gas feed, since greater amounts result in a reduced methanol selectivity [6]. Accordingly, safe and energy-saving low pressure pathways for the methanol production using a higher percentage of CO_2 feeds are highly desirable. Nonetheless, at ambient pressures the use of the industrial $Cu/ZnO/Al_2O_3$ catalyst for methanol synthesis results in significant CO production, which is unwanted as it reduces the yield of methanol and poisons the catalyst. Therefore, a new class of catalyst materials needs to be developed to realize the low-pressure methanol synthesis from CO_2 on a large scale [7].

In recent years, intermetallic compounds, including NiGa alloys have attracted much attention as catalyst materials and represent a fast-growing research field [8]. Not only may they replace costly noble metal catalysts, but they also represent promising catalyst materials systems of improved stability, selectivity and activity for hydrogenating CO_2 into methanol already at ambient pressures [7-14]. Thanks to their different phases and their respectively differently ordered crystal structures, intermetallic compounds allow for the tailoring of the catalytic properties through different structural motifs exposed at the catalyst surface and changes in their electronic structure due to ligand and geometric effects [15, 16]. On the other hand, the broad ranges of different possible structures in these compounds, including also purely metallic phases and oxidized species, poses a significant challenge for the interpretation of catalytic properties in realistic heterogeneous catalysts. Indeed, the coexistence of different species and their evolution under catalyst activation and reaction conditions make it challenging to elucidate the main active species in experimental measurements, as well as to correlate the results of experimental studies with the insights from

theoretical modeling. Available literature thus often provides conflicting evidence about the nature of the active sites.

The NiGa phase diagram is rich, featuring a total of 9 NiGa alloy phases which can be listed as a function of increasing Ga content as follows [17]: α'-Ni_3Ga_1, δ-Ni_5Ga_3, γ-NiGa, ε-NiGa, β-NiGa, Ni_3Ga_4, Ni_2Ga_3, Ni_3Ga_7, Ni_1Ga_5, where NiO and Ga_2O_3 are the corresponding oxide phases. However, special attention has attracted the δ-Ni_5Ga_3 phase. Based on theoretical simulations end experimental evidence, this phase has been suggested to be more catalytically active toward CO_2 hydrogenation at ambient pressures, with a highly suppressed selectivity toward the unwanted CO production [7,10]. Investigations combining density functional theory (DFT), *in situ* X-ray diffraction (XRD), *ex situ* transmission electron microscopy (TEM) and catalytic reactivity measurements indicate that while the Ga-rich sites are responsible for methanol synthesis, the Ni-rich sites are the catalytically active sites toward the production of CO via the reverse water-gas shift reaction (rWGS), which may become suppressed by the poisoning by adsorbed CO [7]. Hence, it has been concluded that an amorphous Ga_2O_3 shell surrounding the NPs might promote the CO_2 activation [6], especially in connection with a metallic phase that activates H_2. The latter has been concluded to result in oxygen vacancies in the Ga_2O_3 which enable CO_2 adsorption and activation [18,19]. Accordingly, synergetic effects for an enhanced methanol production between metallic Ni-Ga sites and the presence of Ga_2O_3 in their vicinity have been concluded [6]. In contrast, an investigation combining X-ray photoelectron spectroscopy (XPS), H_2 and CO temperature-programmed desorption and CO_2 conversion experiments over a model Ga_3Ni_2 single crystal catalyst showed that the pretreatment of the catalyst plays a crucial role for its catalytic activity and that the oxidized catalyst surface decreases the catalytic activity for CO_2 hydrogenation to methanol [16]. These conflicting findings illustrate that the underlying reaction mechanisms for CO_2 hydrogenation and the nature of the active species in the NiGa system are still unclear. Furthermore, a profound understanding of the underlying catalyst phase changes under activation conditions is required, with the aim to optimize activation protocols that stabilize certain phases during the activation process. This is of particular importance for alloy systems that contain non-noble metals with different standard enthalpies for oxide formation, since in this case the surface chemistry is greatly dependent on the catalyst pretreatment. Hence, when the NiGa system is exposed to air, Ga is driven to the surface upon oxide formation, as it is characterized by

a higher oxygen affinity as compared to Ni [16]. However, this typically results in a non-trivial chemical restructuring and heterogeneity of the catalyst, which often cannot be overcome in the activation process. As a consequence, different catalyst pretreatments have shown to have distinct effects on the catalytic performance [[6].

New *in-situ* and *operando* investigations on well-defined NiGa nanocatalysts are thus needed to identify the most catalytically active sites and to find ways to stabilize them during catalyst activation procedures and under methanol synthesis working conditions. Since none of the experimental techniques, when used alone, is able to provide a comprehensive analysis of the complex processes taking place on the different length scales in these heterogeneous catalysts, these studies must rely on multiprobe approaches. Therein, different bulk- and surface-sensitive techniques provide complementary information on the catalyst structure and composition, to be consequently correlated with the results of catalytic measurements.

To this end, we combined *operando* XAS, *operando* XRD, and near ambient pressure XPS (NAP-XPS) with *ex-situ* scanning transmission electron microscopy (STEM) and atomic force microscopy (AFM) to shed light on the phase transitions and chemical compositions of SiO_2-supported size-controlled Ni_5Ga_3 and Ni_3Ga_1 NPs under activation and reaction conditions for methanol synthesis. The well-defined NPs were prepared using an inverse micelle encapsulation technique [20-23]. The use of NPs automatically allows us to bridge the materials gap and to employ a wide variety of surface and bulk-sensitive characterization techniques to gain insight into surface and near-surface changes in the catalyst structure and composition. Furthermore, since it is only the Ni_2Ga_3 compound that is in equilibrium in a binary Ga-Ni melt [6], it also represents the only alloy composition for which the growth of single crystals is feasible. On the other hand, the study of NP systems, synthesized inside micellar cages, allows us to investigate NPs featuring the Ni_5Ga_3 and the Ni_3Ga_1 alloy compositions, which are of interest in the light of prior studies [7,10]. We concluded the as-prepared NPs to consist of crystalline NiO decorated by amorphous and dispersed Ga_2O_3. During the activation of the catalysts at 700°C in 1 bar H_2, metallic Ni was found for both compositions prior to its alloying with Ga. The coexistence of metallic Ni with different NiGa alloy phases is of high importance for explaining the observed catalytic properties of the NPs. Under *operando* conditions we found Ga in both NP compositions to be partially oxidized, forming an oxide shell. Our catalytic activity tests revealed that the Ni_5Ga_3 NPs are

highly active towards the production of methanol (92% selectivity at 210°C), which we ascribed to the presence of δ-Ni_5Ga_3 in this material system. On the contrary, the Ni_3Ga_1 system featured a greatly reduced methanol production and a high selectivity towards the production of methane, likely due to the presence of excess metallic Ni. This work aims to yield a detailed overview on the structural and electronic characteristics of NiGa catalysts with different compositions as a function of the activation and reaction conditions, for which contradictory results are found in the literature [6, 16, 18, 19]. By directly correlating the underlying phases and oxidation states for the two NiGa compositions to the results of our reactivity studies, we identify the role of different species coexisting in this highly heterogeneous catalyst, and pave the road for the further catalyst optimization and future theoretical investigations into the working mechanism of NiGa catalysts.

2 Experimental

2.1 Sample preparation

The NiGa NP samples were prepared using an inverse micelle encapsulation method [20-23]. A PS-S2VP diblock copolymer of the poly(styrene-b-2-vinyl pyridine)(PS-P2VP) series by PolymerSource^{TM} was dissolved in a non-polar solution of toluene, and the solution was stirred for one day. The polar heads (P2VP) attract each other and form cages into which later on the dissolved metal salts are loaded, where the non-polar tails (PS) act as spacers in the solution. As metal salts, gallium(II) chloride and nickel(II) nitrate hexahydrate (Sigma Aldrich) were used and dissolved in tetrahydrofuran (THF) with nominal Ni:Ga atomic ratios of 75:25 for the Ni_3Ga_1 NPs and 62.5:37.5 for the Ni_5Ga_3 NPs. After mixing the two solutions, the resulting mixture was stirred for additional two days, which based on our prior experience with this synthesis method is sufficient time to load the micellar cages with the metal salts [20-23]. Thereafter, the samples were filtered to remove undesired contaminations, including larger metal agglomerates formed in cases of improper dissolution of one of the metal salts into the polymeric micellar solution. The PS and P2VP molecular weights comprised 8200 g/mol and 8300 g/mol, respectively, and the metal salt to P2VP ratio corresponded to 0.2.

To distribute the NP catalysts on a high surface area support, incipient wetness impregnation of the solution onto SiO_2 powder from Strem Chemicals Inc. was carried out. Based on the results obtained from thermogravimetric analysis measurements and using a heating rate of 5 °C/min, the

powder catalysts were thereafter calcined for 6 h in a rotary oven in a gas flow mixture of 80 ml/min O_2 and 300 ml/min N_2 at 450°C for the Ni_3Ga_1 NPs and 470 °C for the Ni_5Ga_3 NPs to remove impurities such as carbon contamination and to drive off chemically bound moisture (see **Figure S1** in the **Supporting Information** for an explanation of the choice of the calcination temperature). After calcination, the metal-content of the powder catalysts was determined by means of inductively coupled plasma-mass spectrometry (ICP-MS). Beforehand, the powder catalysts were dissolved in a 10 ml mixture of HCl:HNO_3:H_2O with a 3:1:1 ratio and heated in a microwave (Anton Paar GmbH, Multiwave GO) at 180°C for 30 min. The ICP measurements revealed a metal catalyst loading of 3.5 and 5.3 wt% (mass fraction) for the Ni_3Ga_1 and the Ni_5Ga_3 samples, respectively. The metal composition of the Ni_3Ga_1 sample was deduced to consist of 80.7% Ni and 19.3% Ga, the Ni_5Ga_3 sample consisted of 58.6% Ni and 41.4% Ga.

In addition to the preparation of the powder catalysts, the NiGa NP solution was also dip-coated onto Si(111) substrates to facilitate the AFM and the NAP-XPS measurements. To ensure a good interaction between the NPs and the support, the polymers were removed after dip-coating by means of an oxygen plasma treatment using a Plasma Prep III etcher from SPI supplies. The applied settings comprised 20 W power, 350 mTorr oxygen pressure and a treatment time of 20 min. The plasma treatment was repeated until the carbon removal was confirmed in the XPS spectra acquired in our lab-based XPS setup (SPECS GmbH). During this plasma treatment, the surface of the Si(111) substrate oxidizes. This results in a thin SiO_2 layer and a sample system consisting of the NiGa NPs supported on SiO_2/Si(111).

2.2 Sample characterization

In situ **and** *operando* **XRD characterization:** The XRD measurements were carried out using a Bruker D8 Advance diffractometer in Bragg-Brentano geometry equipped with a Cu source (X-ray wavelength: 1.5406 Å) and a Lynx-eye-detector. For the *in situ* H_2 activation studies of the powder catalysts, an Anton Paar XRK900 heating chamber was mounted onto the diffractometer stage, which allowed the acquisition of computer-controlled temperature-ramps during the catalytic reaction. During the activation studies, diffraction patterns of two different 2θ ranges were acquired. The long-range scans covered a 2θ range from 15 up to 85°, with a step size of

0.01° and a counting time of 2.5 s. The short-range scans covered a 2θ range of 40-60°, using a step size of 0.01° and a counting time of 2 s. In a second experiment, the step size and counting time comprised 0.015° and 2.5 s for the short-range scans, and 0.015° and 2.2 s for the long-range scans. The main diffraction peaks of the various Ni- and/or Ga- containing structures that have been reported for NiGa systems can be used as typical fingerprints for these individual structures, and occur within a 2θ angle range of 40-60°. This can be deduced from **Figure S2** in the Supporting Information, which shows the simulated diffractograms for various NiGa structures. Hence, by acquiring the diffractograms at each temperature step within this rather narrow 2θ range, the measurement time was minimized to about 60 min per temperature step. Thus, a temporal resolution of around 70 minutes was achieved, which is about two times better in comparison to previous *in situ* studies [10] and allows us to better track the transiently present intermediate species.

The H_2 activation was carried out using 1 bar H_2 and an H_2 flow of 10ml/min with a heating rate of 10°C/min up to 700°C. The long-range scans were performed at room temperature (RT) on the as-prepared catalysts as well as after activation at 700°C and 1 bar H_2. The short-range 2θ scans were performed at 100°C, 200°C, 300°C, 400°C, 500°C, 600°C, and 700°C during the heating ramp.

In addition, *operando* XRD measurements (long-range scans, 15-85°, 0.015° step size, 2.2 s measurement time) were performed during CO_2 hydrogenation at selected temperatures (180˚C, 210˚C, 240˚C, and 300˚C), using a total pressure of 1 bar, a total flow of 10 ml/min, and an H_2:CO_2 ratio of 3:1.

All XRD data were analyzed by means of Rietveld refinement using the Bruker software package TOPAS [24]. The XRD results for the samples' phase concentration, lattice parameters and crystalline sizes under activation in H_2 correspond to the mean values of the two sets of XRD measurements. The error bars correspond to the respective standard deviation.

***Operando* XAS measurements:** The *operando* XAS measurements were performed at the CLAESS beamline at the ALBA synchrotron in Barcelona, Spain [25]. A multipurpose *in situ* cell for high-temperature solid-gas reactions was used for the *operando* measurements. The powder catalysts were mixed with boron nitride, pressed into 5 mm disks and mounted into the cell. The measurements were performed in transmission mode at the Ni K-edge (8 333 eV) and the Ga K-

edge (10 367 eV). A fully tuned Si(311) monochromator was used for energy selection, a reflective mirror was employed for rejecting the higher harmonics. The intensity before and after the samples was measured using ionization chambers filled with a 97.4% N_2 and 2.6% Kr mixture (I_0 chamber) or a 50.5% N_2 and 40.5% Kr mixture (I_1 chamber). For the *in situ* XAS investigation during activation under H_2 flow (20 ml/min), XAS spectra were continuously collected, while the temperature was stepwise increased up to 620°C (maximal achievable temperature in this setup), where the total pressure was held constant at 1 bar. After the activation, the sample was cooled down to RT while maintaining the H_2 atmosphere, followed by a collection of high quality XAS data. The sample was thereafter exposed to reaction conditions (CO_2 and H_2 1:3 mixture with a total gas flow of 80 ml/min), while the temperature was gradually increased up to 250°C using a heating rate of 10 °C/min. XAS data were continuously collected during this process. After that, the sample was cooled down to RT and the collection of high-quality XAS data was repeated.

Ni K-edge XAS spectra for NiO and Ni foils and a Ga K-edge spectrum for Ga_2O_3 were collected as references for the Ga K-edge. The XAS spectra were aligned, normalized and X-ray absorption near edge structure (XANES) and extended X-ray absorption fine structure (EXAFS) data were plotted using the ATHENA software [26]. The analysis of the edge-steps at the Ni and Ga K-edges was used to determine the relative Ni to Ga ratios in both samples. Linear combination analysis (LCA) was performed for the interpretation of the XANES data. The EXAFS data analysis was performed using a non-linear least-square fitting as implemented in the FEFFIT code [26]. The conventional EXAFS analysis was complemented by an advanced artificial neural-network-based approach [27-29] to facilitate the analysis of the high-temperature data, for which anharmonic thermal atomic motion affects the shape of the bond-length distribution [30-32] and introduces artifacts in conventional EXAFS analysis. Moreover, the neural-network based approach was used to analyze the contributions of distant coordination shells, which are more informative for distinguishing different alloy phases [27, 28], but cannot be easily interpreted using conventional approaches.

Catalytic testing: The catalytic activity of the samples was tested in a packed-bed mass flow reactor connected to a gas chromatograph equipped with both, flame ionization (FID) and thermal conductivity detectors (TCD). For the testing, 40 mg of the Ni_3Ga_1 and Ni_5Ga_3 powder catalysts were packed inside a quartz tube and fixed on both sides with two pieces of quartz wool. The

reactor provides independent inlets for various gases in a pressure range of up to 100 bar. For this work, a total constant pressure of 1 bar was used. Prior to the catalytic reactivity tests, the powder catalysts were reduced/activated for 7.5 h at 700°C in a 10 ml/min flow of H_2 at a total pressure of 1 bar (heating rate: 10°C/min). Thereafter, the sample was cooled down to 160°C under the same H_2 flow conditions prior to starting the catalytic reactivity tests at selected reaction temperatures (160°C, 180°C, 210°C, 240°C, 250°C, 300°C). The composition of the reaction products was monitored by sequential gas injections performed during a time span of at least 7 h at each of the reaction temperatures. The catalytic testing was carried out in a reaction mixture of CO_2 and H_2 at 1 bar total pressure, with a CO_2:H_2 stoichiometric ratio of 1:3, corresponding to the direct hydrogenation of CO_2 into methanol. A gas hourly space velocity (GHSV) of 8000 ml/(g·h) was used in each case to facilitate a direct comparison to previous studies [6], resulting in a total CO_2+H_2 flow of 5.33 ml/min for both catalyst samples.

NAP-XPS measurements: The NAP-XPS measurements were carried out at the National Synchrotron Light Source II (NSLS II), New York, USA at beamline 23-ID-2 IOS, which is dedicated to *in situ* and *operando* soft X-ray spectroscopy studies at pressures up to 13 mbar and which operates in an X-ray photon energy range of 0.25-2.0 keV. To obtain information on possible segregation effects under activation and reaction conditions with the pressure ranging between 0.7 and 2.1 mbar, we alternated in our NAP-XPS measurements between the photon energies of 1250 and 1540 eV. The binding energy of the Ga 2p spectra yielded the lower limit (1250 eV) of the used photon energy range, the upper limit (1540 eV) was determined by the characteristics of the beamline monochromator employed and the photon flux required. The use of the two different photon energies thus allowed us to vary the inelastic mean free path of the photoelectrons between 0.6-1.2 nm for the Ga 2p spectra and 0.8-1.1 nm for the Ni 2p spectra, as can be inferred from Ref. [33], and accordingly the probing depth. For the NAP-XPS measurements, the Ni_5Ga_3 and Ni_3Ga_1 NPs were dip-coated onto SiO_2/Si wafers. Prior to NP deposition, these Si substrates had undergone an oxygen plasma treatment at 350 mTorr O_2 for 20 minutes using a power of 30 W. The NAP-XPS data were analyzed using the software CasaXPS [34], calibrating the Ga 2p and Ni 2p spectra to the Si 2p oxide binding energy.

Ex situ **microscopy measurements:** AFM measurements were performed using a Multimode 8-HR setup from Bruker employing air tapping mode and CT 300 R cantilevers from Team

Nanotec (f_0=300 kHz, k=40 N/m). All AFM data have been analyzed using the open source software Gwyddion [35]. The morphology of the as-prepared powder catalyst samples after calcination was investigated by STEM and energy-dispersive X-ray spectroscopy (EDX) using a JOEL JEM-2800 setup.
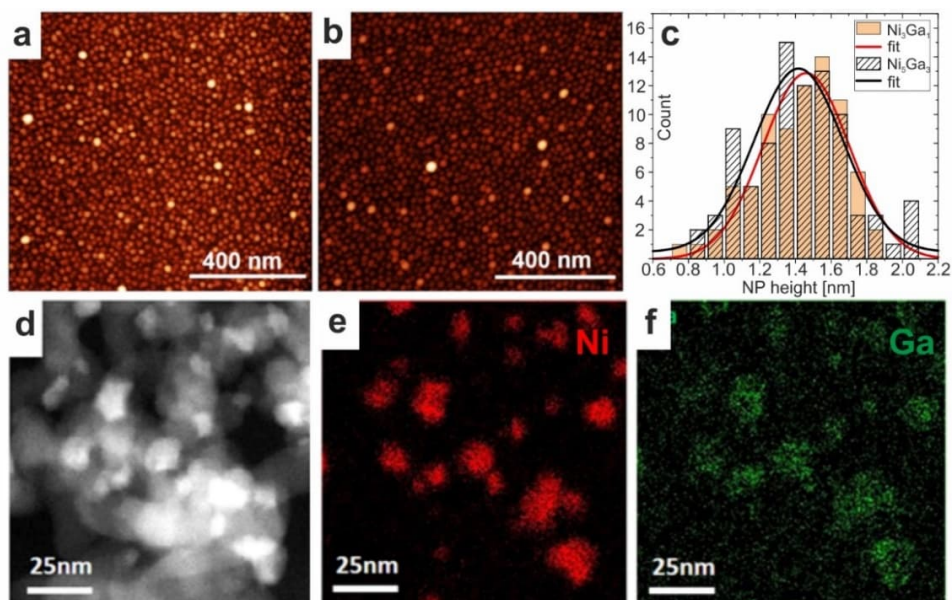

Figure 1: Images of bimetallic NiGa NPs. AFM image of Ni_5Ga_3 (a) and Ni_3Ga_1 (b) with the respective NP height distributions shown in (c). (d): STEM image and EDX distribution maps for Ni (e) and Ga (f) for the Ni_3Ga_1 sample after calcination.

3 Results

3.1 As-prepared NiGa NPs prior to H_2 activation and reaction conditions

Figure 1 shows typical AFM images obtained on the as-prepared Ni_5Ga_3, **Figure 1(a)**, and Ni_3Ga_1, **Figure 1(b)**, NPs and confirm the existence of NPs with a narrow size distribution. The data analysis of the images revealed NP sizes (heights) of 1.4 ± 0.4 nm and 1.5 ± 0.6 nm for the Ni_5Ga_3 and the Ni_3Ga_1 NPs, respectively, **Figure 1(c)**. Note that the NPs in the AFM measurements correspond to particles deposited on planar systems, that have not been calcined and have accordingly not undergone calcination-induced sintering. Thus, the average particle sizes deduced from the AFM images are smaller as compared to the sizes (TEM diameters) of the calcined powder catalyst NPs. In addition to the AFM measurements, STEM images were

acquired, **Figure 1(d)**, and energy-dispersive X-ray (EDX) distribution maps were collected on the powder catalysts after calcination, see **Figure 1(e,f)**, to confirm the elemental distribution of Ni and Ga on the Ni_3Ga_1 catalysts. Note the larger NP diameters (typically 10-15 nm) of the calcined powder catalyst in the STEM images as compared to the NP heights deduced from the AFM measurements. Since the micellar NP precursors usually lead to spherical NPs, the difference between the AFM NP heights and TEM NP diameters must be related to sintering taking place during the annealing treatment in synthetic air up to 470°C on the NiGa NPs deposited on the nanocrystalline SiO_2 supports prior to the reaction. Note that the same type of planar NP samples as used for the AFM measurements were also used for the *operando* NAP-XPS measurements discussed in section 3.3.1.

3.2 Phase transitions under activation and working conditions

Prior to their operational use, catalysts undergo an activation procedure in which the initially oxidized catalyst particles become reduced. The phase changes that the particles undergo during this pretreatment as well as the resulting catalyst phase have been discussed to greatly influence the catalytic activity [15]. Accordingly, it is of utmost importance to understand the phase transitions as a function of the catalyst pretreatment conditions, and to be able to stabilize the desired catalyst phases.

In the present work we used *in situ* powder XRD and XAS to unravel the phase changes of size-controlled Ni_5Ga_3 and Ni_3Ga_1 NPs impregnated on SiO_2 powder during activation under annealing in 1 bar of H_2.

3.2.1 *In situ* and *operando* XRD under activation and working conditions

To investigate the phase changes of the NP catalysts under H_2 activation, XRD patterns were recorded under selected temperatures during the stepwise annealing of the samples from RT up to 700°C under 1 bar H_2.

The unit cells of the possible structural phases of the NiGa system are depicted in Figure **2(a)**. NiGa phases of higher Ga concentration are unlikely, since Ga is more prone to oxidation, leading to the formation of Ga_2O_3, and the consequent depletion of Ga in the metal alloy NP, resulting in a shift towards more Ni-rich phases [17]. **Figure 2(b,c)** shows the XRD patterns acquired for the

Ni$_3$Ga$_1$ and the Ni$_5$Ga$_3$ samples, and **Figure 3(a,d)** compares the corresponding percentage of the individual structural phases deduced from the fits to the data based on a Rietveld refinement. To ensure that other crystalline phases were not missed, extended 2θ scans (15-85°) with a longer acquisition time (total measurement time 3 h 40 min) were acquired at RT prior to the H$_2$ activation, **Figure S3(a,c)**, also in H$_2$ at 700°C just after reaching the temperature, as well as after 4.5 h under these conditions (**Figure S3(b,d)**).

For both samples, Ni$_3$Ga$_1$ and Ni$_5$Ga$_3$, the long-range XRD patterns measured on the as-prepared samples at RT showed Bragg peak positions that are in line with the presence of NiO crystallites only, indicating that for both NiGa compositions the NPs were in a completely oxidized state. The sizes of the NiO crystallites comprise ~15.5 nm and 7.5 nm for the Ni$_3$Ga$_1$ and the Ni$_5$Ga$_3$ samples, respectively, as was determined from the fits to the experimental data using the Rietveld refinement, see **Figure S3(a,c)**. The absence of diffraction signals from Ga$_2$O$_3$ implies that the Ga oxide phase was highly X-ray amorphous and dispersed in the as-prepared state of the samples. This observation agrees with previous findings based on combined NAP-XPS, environmental TEM, high energy resolution fluorescence-detected XAS, thermal programmed desorption and XRD investigations for 6-7 nm sized NiGa catalysts prepared using incipient wetness impregnation of a mixed aqueous solution of Ni and Ga nitrates on silica [6].
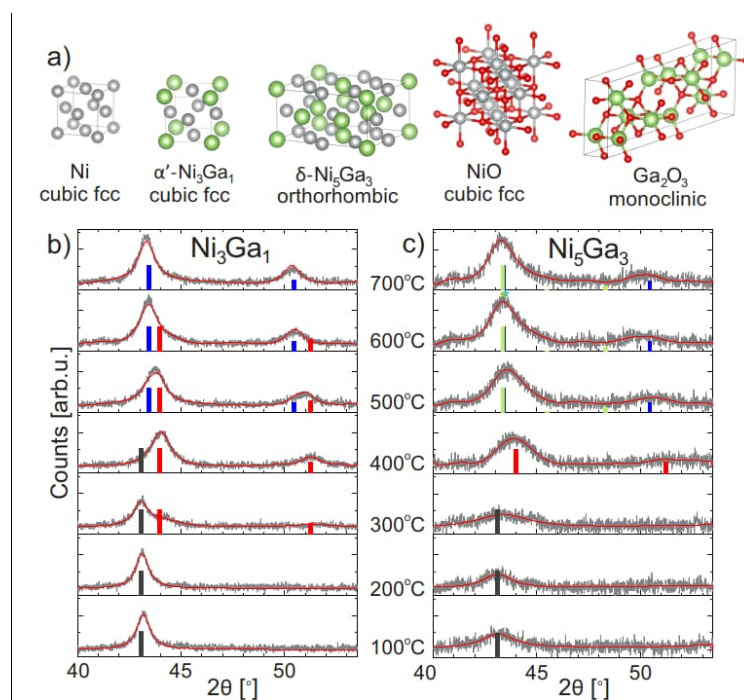
Figure 2: *(a): Unit cells of Ni- and Ga containing phases that have been reported for the NiGa system. (b,c): XRD patterns (black lines: experimental data, red lines: fit to the data based on Rietveld refinement) measured under 1 bar H_2 at different temperatures for the (b) Ni_3Ga_1 and the (c) Ni_5Ga_3 samples. The positions of the Bragg peaks are indicated by line references in black (NiO), red (Ni), blue (α'-Ni_3Ga_1) and green (δ-Ni_5Ga_3).*

During the initial temperature steps of the catalyst activation, under annealing in H_2 at 100°C and 200 °C, only diffraction peaks belonging to NiO (2θ=43.1º) are discernible for both samples, as can be deduced from **Figure 2(b,c)**. As the NiO crystallites also maintain their respective sizes, it can be assumed, that the particles in both samples are still completely oxidized under these conditions. It is only at 300°C that for the Ni_3Ga_1 sample additional diffraction signals attributed to metallic Ni appear (2θ=44.05, 2θ=51.2º). At 400°C the diffraction signals from metallic Ni are strongest, signaling an almost complete reduction of the Ni_3Ga_1 sample. Contrary, for the Ni_5Ga_3 NPs, the reduction from NiO to Ni starts only at 400°C, where the sample is relatively quickly completely reduced to metallic Ni at the same temperature step.

For both NiGa samples, the annealing under 1 bar H_2 at temperatures higher than 400°C resulted in a shift of the diffraction signals in (**Figure 2(a,b)**) toward lower scattering angles. By comparing this trend with the positions of the main Bragg peaks in the simulated diffractograms of the different NiGa reference structures (**Figure S2**), we reveal that this shift is related to the formation of NiGa alloy phases. This implies that the initially amorphous Ga oxide (invisible in the XRD data directly) becomes increasingly reduced with the resulting metallic Ga progressively being incorporated into the metallic Ni to form NiGa alloys. Thus, in the case of the Ni_3Ga_1 NP sample, the diffraction patterns acquired at 500°C and 600°C in H_2 can be explained by the coexistence of metallic Ni with a metallic α'-Ni_3Ga_1 alloy (2θ=43.4º, 2θ=50.5º), where the respective weight of the latter phase increases with temperature (**Figure 3(a)**). At 700°C, the diffraction pattern is best reproduced assuming the presence of the α'-Ni_3Ga_1 phase only, with no signatures of the metallic Ni phase detected, see **Figure S3(b)**. Contrary, in the case of the Ni_5Ga_3 NP sample, which featured 100% metallic Ni at 400°C, the diffraction patterns acquired under 500°C, 600°C, and 700°C can only be explained in the Rietveld analysis by the coexistence of the α'-Ni_3Ga_1 and δ-Ni_5Ga_3 alloy phases, with respective weights of about 60% and 40%. This is because, in contrast to the Ni_3Ga_1 sample, the relative peak intensity ratio between the diffraction

peaks at around $2\theta=43.4°$ and $2\theta=50.5°$ is increased under these conditions. This observation can only be explained by the presence of the δ-Ni_5Ga_3 phase, which yields an additional intensity contribution at $2\theta=43.3°$. It should be noted that for the δ-Ni_5Ga_3 phase a low-intensity diffraction peak at $2\theta=48.3°$ is anticipated, which is, however, not distinguishable in our data. We assume that the peak signal is below the noise level of the experimental data due to the small particle sizes and their highly disordered structure (see below). Moreover, the δ-Ni_5Ga_3 phase amounts to a maximum relative phase concentration of only 40%.

The data, moreover, indicate a tendency for the percentage of the δ-Ni_5Ga_3 phase ($2\theta=43.3°$, $2\theta=48.3°$) to slightly increase as a function of temperature and/or time. Thus, the analysis of the extended-range diffractograms that were taken 4.5 h after having reached 700°C under H_2, **Figure S3(d)**, revealed the presence of catalyst particles that contained 53±4% of the α'-Ni_3Ga_1 phase and 47±7% of the δ-Ni_5Ga_3 phase, indicating that more Ga was incorporated into the alloy structures under these conditions over time.

To obtain a more detailed insight into the restructuring process of the nanocatalysts under activation, the lattice parameters along with the crystallite sizes as obtained from the Rietveld refinement for the individual phases are plotted for the Ni_3Ga_1 and the Ni_5Ga_3 samples in **Figure 3(c,d)** and **Figure 3(e,f)**, respectively. The refinement parameters are summarized in **Tables S1** and **S3** of the Supporting Information.

Overall, the obtained lattice parameter values for the different constituent phases observed in our XRD experiments are in a good agreement with the values found in the literature. The only discrepancies were evidenced for the δ-Ni_5Ga_3 phase, having a lattice parameter a approximately 5% larger, while the lattice parameter c is ca 5% smaller than the literature data, implying a distortion of the orthorhombic δ-Ni_5Ga_3 similar to that created by the Poisson effect. It describes the phenomena in which a material expands perpendicular to the direction of its contraction.

Regarding the crystallite sizes, it is striking that for both samples the crystallite size shrinks dramatically when the NiO is fully reduced to metallic Ni at 400°C (for the Ni_3Ga_1 sample it reduces ca 36%, from 13.9±1.4 nm to 8.9±1.0 nm; for Ni_5Ga_3 ca 20%, namely, from 5.15±0.25 nm to 3.8±0.7 nm). Considering the different metal packing density within the NiO and Ni unit cells, a full reduction from NiO to Ni should result in a shrinkage of the crystallite size by only 16%. Accordingly, the observed size decrease can only partially be ascribed to the reduction and

it can be assumed that the crystallites become fragmented and increasingly dispersed in the reduction process. With increasing temperature and the progressive incorporation of Ga, the crystallite sizes increase again for both NiGa samples. Considering the size and the original metal packing density of the metallic Ni crystallites, the α'-Ni$_3$Ga$_1$ crystallites that form thereafter feature for both samples a size which is about 25% larger than that expected for the bulk alloy crystallites that can form by the incorporation of Ga into the initial Ni crystallites. Similarly, the crystallites of the δ-Ni$_5$Ga$_3$ phase inside the Ni$_5$Ga$_3$ sample were found to be 12% larger than expected. This indicates that for annealing temperatures of 500°C and higher, NP sintering occurs for both samples and their bulk-like NiGa alloy phases. Sintering can be expected in this temperature range since the highest calcination temperature was for both samples below 500°C. Yet, the crystallite size increase can also be traced back to the progressive incorporation of Ga into the crystallites under these elevated temperatures.
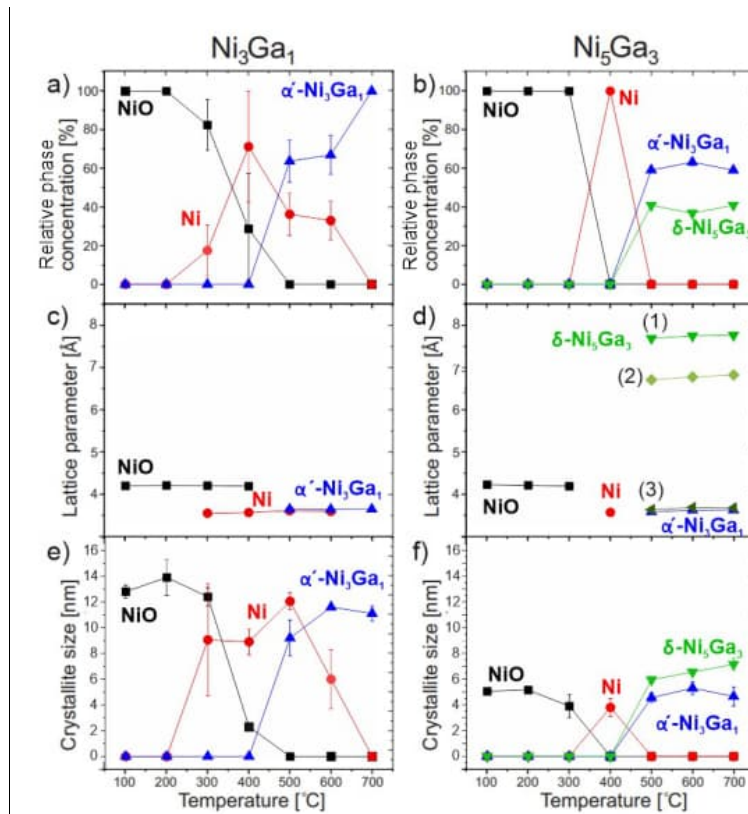

Figure 3: *Relative phase concentrations (a, b), lattice parameters of the different phases (c, d), and their crystallite sizes (e, f) for the Ni$_3$Ga$_1$ (a,c,e) and Ni$_5$Ga$_3$ sample (b,d,f) as obtained from the Rietveld analysis of XRD data collected in 1 bar H$_2$. The XRD results correspond to the mean values of two sets of*

*measurements summarized in **Tables S1** and **S3** in the Supporting Information. The calculation of the relative phase concentration considers only the ordered phases detectable by XRD (NiO, Ni, α'-Ni$_3$Ga$_1$, δ-Ni$_5$Ga$_3$). The error bars correspond to the respective standard deviation. (1)-(3) in (d) represent the experimental lattice parameters a, b, and c of the orthorhombic δ-Ni$_5$Ga$_3$ phase. The experimental lattice parameters agree well with the theoretical ones given as follows [36-39]: NiO: a=4.2166 Å, Ni: a=3.5058 Å, Ni$_3$Ga$_1$: a=3.5744 Å, Ni$_5$Ga$_3$: a=7.5024 Å, b=6.8022 Å, and c=3.7159 Å.*

Operando XRD data measured on the sample during CO_2 hydrogenation reaction conditions were also collected. **Figures S4** and **S5** show the fit to the data obtained from the Rietveld refinement, the corresponding refinement parameters are summarized in **Tables S5** and **S6**. For both alloy compositions we found a shift of the diffraction angle positions toward higher diffraction angles when switching to CO_2 hydrogenation reaction conditions. For the Ni$_3$Ga$_1$ sample the shift can only be explained by the coexistence of the α'-Ni$_3$Ga$_1$ phase and metallic Ni. The relative phase concentration of the latter was found to decrease with increasing reaction temperature, ranging from 67% at 180°C to 43% at 300°C. Contrary, in the case of the Ni$_5$Ga$_3$ sample, the diffraction data collected under reaction conditions indicate the coexistence of the α'-Ni$_3$Ga$_1$ and the δ-Ni$_5$Ga$_3$ phase, with a higher percentage of the α'-Ni$_3$Ga$_1$ phase compared to that observed for the sample reduced in H_2.

3.2.2 *In situ* and *operando* XAS under activation and working conditions

A disadvantage of XRD is that it only allows for tracking the evolution of structurally well-ordered phases. Moreover, the contribution of large ordered particles dominates the XRD data. Therefore, to gain further insight into the evolution of the nanocatalysts under H_2 activation and to track their chemical state and structure, complementary *in situ* XAS measurements were performed at the Ni and Ga K-edges. Furthermore, the catalyst structure and chemical state were probed by *operando* XAS under CO_2 hydrogenation conditions. The XANES and Fourier-transformed EXAFS data obtained are shown in **Figures 4** and **5**, respectively, as well as in **Figure S6** and **Figure S7**. The analysis of the X-ray absorption jumps at the Ni K-edge and the Ga K-edge suggests a Ni to Ga ratio of 6.4 to 3 for the Ni$_5$Ga$_3$ sample, and of 3.8 to 1 for the Ni$_3$Ga$_1$ sample, which is close to the nominal Ni to Ga ratios in these samples, but suggests slight excess of Ni in both samples. As it can be inferred from these XANES and EXAFS spectra, the as-prepared NiGa

NPs in both samples are initially fully oxidized and exhibit a NiO-like local structure for the Ni species, in line with our XRD data. The Ga K-edge XANES data, in turn, resemble the reference spectrum for Ga_2O_3, but the noticeable differences in the intensity of the main XANES features, and the suppressed contribution of distant coordination shells for the NiGa NPs in comparison to the Ga_2O_3 reference, suggest a strong distortion of the Ga local structure. A non-linear least-square fitting of the EXAFS data was performed, with the results summarized in **Figures S8** and **S9** and **Tables S7** and **S8**. They show an excellent quantitative agreement between the Ga-O, Ni-O and Ni-Ni bond-lengths and the coordination numbers for the as prepared NiGa NPs with respect to those parameters in the NiO and the Ga_2O_3 reference materials. Details of the EXAFS data fitting are given in the **Supplementary Note 2**.

Upon catalyst activation in H_2, both, the XANES and the EXAFS spectra, changed drastically as shown in **Figure 4(a,b)** and **Figure 5(a)** for the Ni_5Ga_3 sample, and **Figures S6-S8** for the Ni_3Ga_1 sample. For both, the Ni and the Ga K-edges, the acquired spectra shifted gradually toward lower photon energies, which is a clear sign of sample reduction. The peak in the FT-EXAFS at ca. 1.5 Å (phase-uncorrected), which is attributed to a Ga-O or Ni-O bond contribution, was found to decrease with time (**Figure 5(a,b)** and **Figure S8**), while a new peak at ca. 2.0 Å appears both in the Ni K-edge and the Ga K-edge EXAFS, indicating the formation of Ni-M and Ga-M bonds. Here M is Ni or Ga and since these elements are located nearby in the Periodic Table, we cannot distinguish between their contributions to the EXAFS spectra.

LCA of our XANES data was used to track the reduction of the Ni and Ga species. For the Ni K-edge XANES LCA, we used spectra for a Ni foil and for NiO as references. For the Ga K-edge XANES LCA, we used as references the spectra for the as-prepared and fully reduced Ni_3Ga_1 sample, both collected at RT. The lack of a significant contribution of the oxide species to the latter was confirmed by our EXAFS data analysis as discussed below. Representative examples of the Ni K-edge and Ga K-edge LCA fits are shown in **Figure S9**. The evolution of the fractions of the reduced Ni and Ga species for the Ni_3Ga_1 and Ni_5Ga_3 samples, as determined from the XANES LCA, is summarized in **Figures 6(a)** and **6(b)**, respectively. In addition to the LCA of the XANES data, we performed also EXAFS data fitting for both samples after reduction in H_2 and cooling to RT without exposure to air (**Figures S10** and **S11** and **Table S7** and **S8**). Both XANES and EXAFS

analysis confirm that Ni is completely reduced in both samples, with a sudden increase in the content of reduced Ni species at ca. 400°C (Ni_5Ga_3 sample) or 350°C (Ni_3Ga_1 sample). The reduction temperatures for Ni thus match well those observed by XRD. Note, however, that the XAS data were continuously acquired while the temperature was being ramped up, which makes difficult to assign a precise temperature value to a given XANES spectrum. Our analysis of the XAS data also reveals a reduction of the Ga species. The latter starts at lower temperatures than that of the Ni species, but proceeds more slowly later on. A nearly complete reduction of Ga in the Ni_3Ga_1 sample is achieved at ca. 600°C. For the Ni_5Ga_3 sample, however, ca. 10%-20% of the Ga species remain in an oxidized state according to our XANES and EXAFS analysis, even after exposure to the highest temperature achievable in our experiment (ca. 620°C) for more than 2 hours. It is noteworthy that our bulk-sensitive XAS data indicate that the degree of Ga oxidation for the Ni_5Ga_3 sample remains very similar also under CO_2 hydrogenation conditions (see **Figure 6(b)** condition (II)). According to the fitting of the Ni K-edge EXAFS data collected at RT for both NiGa samples after reduction and subsequent cooling, the Ni-M distance is noticeably longer than the Ni-Ni distance in pure Ni, and is close to the Ga-M distance obtained from the Ga K-edge EXAFS fitting for the NiGa NPs. The latter signals the formation of a NiGa alloy phase with expanded lattice constant with respect to that of pure Ni.

To understand the reduction of the Ni and Ga species in more detail, we used a neural-network (NN) based analysis for the temperature-dependent Ni and Ga K-edge EXAFS data. The NN method allows for inverting the EXAFS spectra and for directly extracting the Ni-M, Ni-O, Ga-M and Ga-O partial radial distribution functions (RDFs), and thus, allows us to follow their evolution in our experiment [29]. The details of the NN-EXAFS approach and its validation on reference structures is given in **Supplementary Note 2** and **Figure S12**. The temperature-dependent RDFs extracted are shown in **Figure S13**. **Figures 7** and **8** compare the RDFs extracted for the as-prepared and reduced Ni_5Ga_3 and Ni_3Ga_1 samples. To quantify the reduction of the Ga and Ni species, we integrated the areas under the first peaks in the M-M and M-O RDFs, and thus extracted the coordination numbers for the Ni-M, Ga-M, Ni-O and Ga-O coordination shells (**Figure 8(a)** for the Ni_5Ga_3 sample, and **Figure S14** for the Ni_3Ga_1 sample) [28]. Unlike conventional EXAFS fitting, the NN-EXAFS-based approach for coordination number

determination can also be reliably used for the interpretation of high-temperature EXAFS data. In agreement with our XANES and EXAFS fitting analysis, the NN-EXAFS shows the reduction of the Ni and Ga species, as evidenced by the decrease of the peaks in the Ga-O and Ni-O RDFs and the Ga-O and Ni-O coordination numbers, paralleled by an increase in the Ni-M and Ga-M RDF peaks and the Ni-M and Ga-M coordination numbers. In the final reduced state, coordination numbers close to 12 were obtained for the Ni species, suggesting their complete reduction and the formation of a nearly close-packed metallic phase. For the Ga species, the increase of the Ga-M coordination number is slower, and for the Ni_5Ga_3 sample the presence of a non-negligible Ga-O bond contribution, and a Ga-M coordination number lower than 12, confirms the presence of oxide species even at the highest temperature.
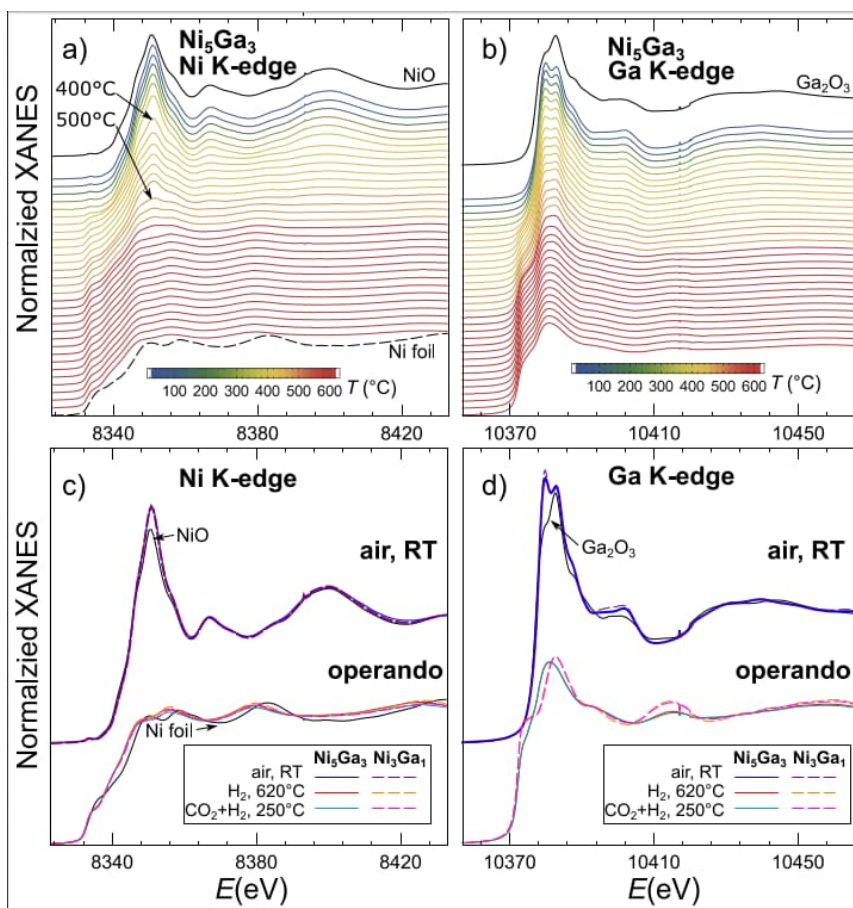

Figure 4: In situ XANES spectra measured for the Ni_5Ga_3 sample at the (a) Ni K-edge and (b) the Ga K-edge during the reduction in H_2. Ni K-edge (c) and Ga K-edge (d) XANES for the as-prepared and reduced Ni_5Ga_3 and Ni_3Ga_1 samples, as well as for the samples under CO_2 hydrogenation conditions at ambient

pressure at 250°C. Spectra are shifted vertically for clarity. Reference spectra for a Ni foil, NiO and Ga₂O₃ are also shown. Note that the XANES spectra in (c) and (d) overlap almost completely for both NiGa samples, which are in the as-prepared state (activated state) both completely oxidized (reduced).
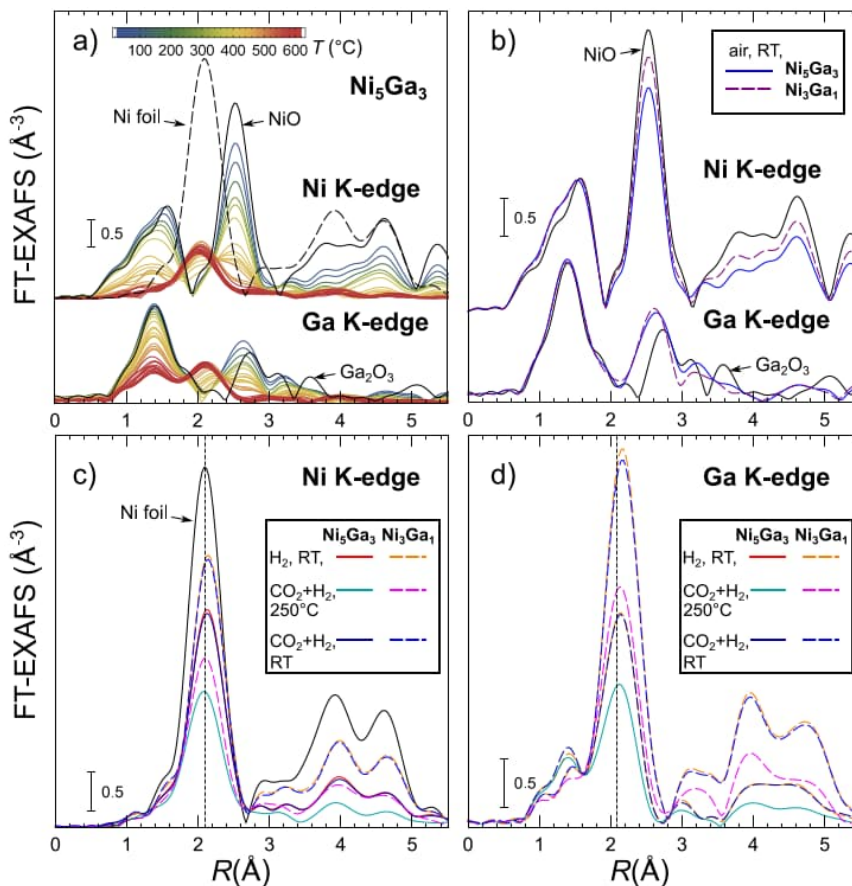

Figure 5: *(a) Fourier-transformed (FT) in situ EXAFS spectra measured for the Ni₅Ga₃ sample at the Ni K-edge and Ga K-edge. (b) Ni and Ga K-edge EXAFS for the as-prepared Ni₅Ga₃ and Ni₃Ga₁ samples. Ni K-edge (c) and Ga K-edge (d) EXAFS for the reduced samples at RT, for the samples under CO₂ hydrogenation conditions at 1 bar at 250°C, and for the samples after reaction cooled to RT. Spectra are shifted vertically for clarity. Reference spectra for a Ni foil, for NiO and Ga₂O₃ are also shown. Vertical line in (c,d) shows the position of FT-EXAFS maximum for Ni foil.*

Figure 7(b) shows clearly that the position of all RDF peaks in the reduced NiGa samples is shifted to higher interatomic distances with respect to that of pure Ni, in agreement with the formation of a NiGa alloy. The evolution of the RDF peak maximum (most probable Ni-M and Ga-M distance) is shown in **Figure 8(b)** (for the Ni₅Ga₃) and **Figure S14** (for the Ni₃Ga₁ sample). We observed that upon heating in H_2, the Ni-M distance gradually increases. Whereas at the

beginning of the reduction the Ni-M distance is similar to that in metallic Ni, during the activation in H_2 it expands by ca. 0.06 Å. At the same time, the Ga-M distance remains approximately the same during the activation. This, together with the slower reduction of the Ga oxide species observed, suggests that the reduced Ni species first form a pure Ni phase, which is then gradually enriched by Ga species forming a NiGa alloy phase. This finding agrees well with the formation of an intermediate Ni phase, as observed in our XRD measurements.
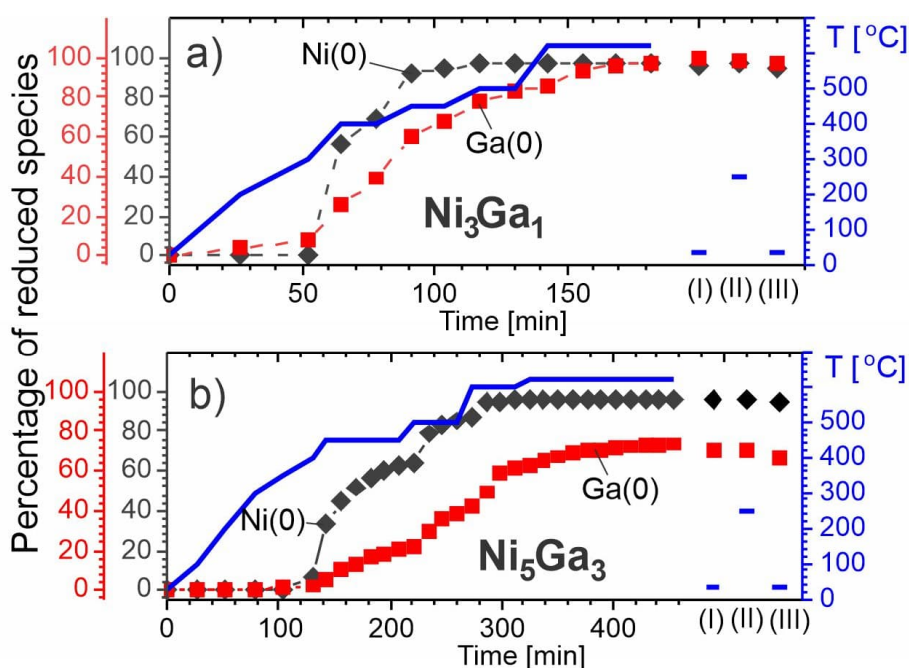

Figure 6: *Fractions of metallic Ni (black) and Ga species (red) as deduced from the LCA of time-dependent XANES data collected at the Ni and Ga K-edges for the (a) Ni_3Ga_1 sample and (b) the Ni_5Ga_3 sample during the reduction in 1 bar H_2. Results obtained from XANES spectra collected at RT after reduction (I), under CO_2 hydrogenation reaction conditions at ambient pressure at 250°C (II) and after reaction at RT (III) are also shown. Time-dependencies of the sample temperature are shown with blue lines.*

A striking difference between the Ni_5Ga_3 and Ni_3Ga_1 samples lies in the shape of the more distant RDF peaks for the reduced phase. These peaks are particularly sensitive to differences in the crystallographic phases [27,28]. Indeed, while for the Ni_3Ga_1 sample the RDF resembles that of metallic Ni (with all peaks shifted to larger interatomic distances), suggesting the formation of an fcc-like structure (e.g., the α'-Ni_3Ga_1 phase), for the Ni_5Ga_3 sample both, Ni-M and Ga-M RDF peaks are significantly broadened, and, crucially, the 3rd and 4th RDF peaks merge together at an

R value of ca. 4.5 Å. The latter is a fingerprint of a non-fcc alloy formation [27], and can thus be associated with the formation of the δ-Ni_5Ga_3 phase.
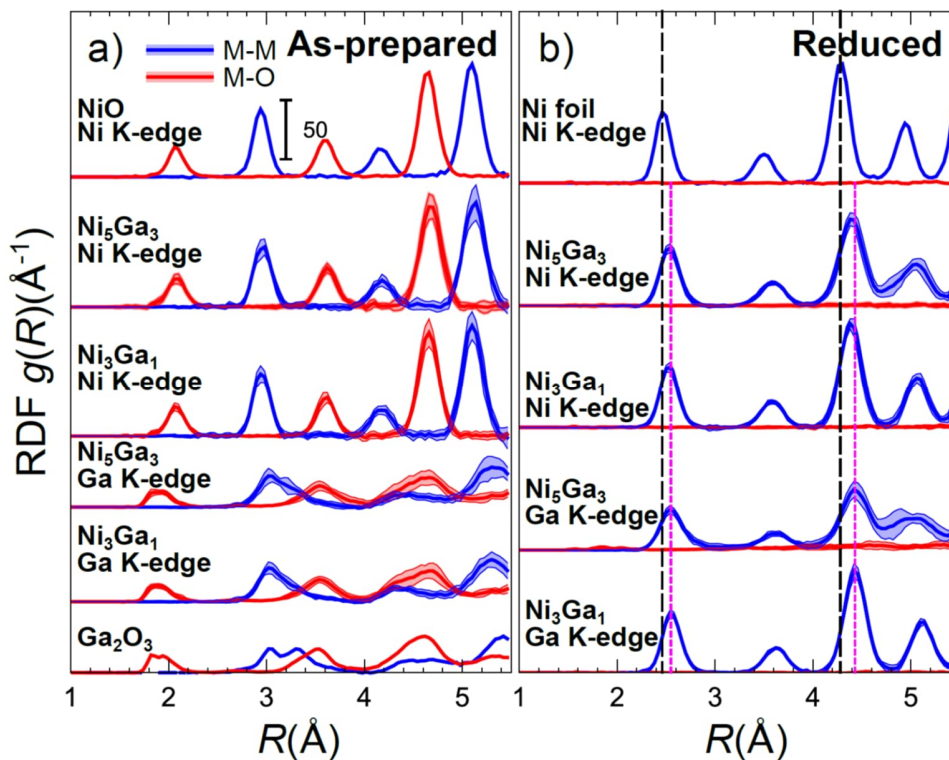

Figure 7: *Partial Ni-O, Ni-M, Ga-O and Ga-M RDFs (here M=Ni or Ga), obtained by NN-EXAFS analysis for the as-prepared (a) and reduced (b) Ni_5Ga_3 and Ni_3Ga_1 samples at ambient pressure at RT. RDFs extracted for reference materials (NiO, Ga_2O_3, Ni foil) are also shown. Vertical dashed lines in (b) show the Ni-Ni distance in metallic Ni (black dashed line) and the final Ga-M distance in the reduced NiGa samples (magenta dashed lines).*

Regarding the structure of the samples under working CO_2 hydrogenation conditions, visual examination of the XANES (**Figure 4(c)**) and EXAFS (**Figure 5(c)**) data suggests that the overall structure of the sample does not change significantly with respect to the fully reduced state. Our LCA-XANES analysis indicates only a slight increase in the concentration of oxidized Ga species in the Ni_5Ga_3 sample (**Figure 6**), while the changes in the Ga-O bonds contribution to the EXAFS spectra are within the uncertainty of our analysis (**Figures S10** and **S11** and **Table S7** and **S8**). No significant changes were observed also in the shape of the RDFs (**Figure S15**), as yielded by our NN analysis of the EXAFS data collected under reaction conditions at 250°C, except the

broadening of the peaks due to an increased thermal disorder. Indeed, after the samples were cooled to RT, the shapes of all RDF peaks were almost indistinguishable from those of the reduced samples. This may suggest that the changes in the NiGa catalyst structure (if any) under working conditions are limited to the catalyst surface only, thus requiring to use a more surface-sensitive technique (such as NAP-XPS) for their quantification.
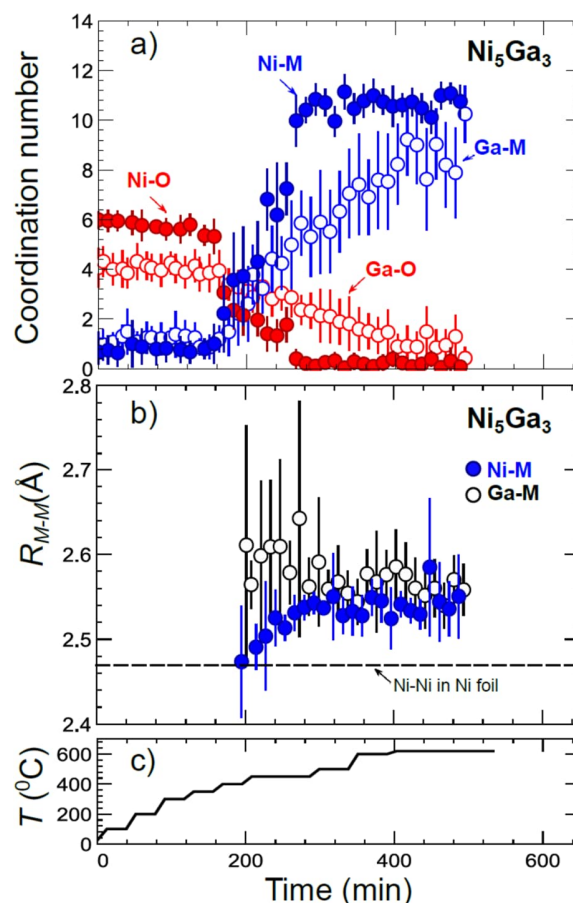

Figure 8: *(a) Evolution of the coordination numbers during activation in 1 bar H_2, as obtained by integration of Ni-O, Ni-M, Ga-O and Ga-M RDF peaks for the Ni_5Ga_3 sample. (b) Evolution of the Ga-M and Ni-M distances in the Ni_5Ga_3 sample during activation in H_2. Corresponding changes in the sample temperature are shown in (c).*

3.3 Catalyst testing and NAP-XPS characterization under methanol synthesis reaction conditions

3.3.1 Surface chemistry and oxidation state evolution

Both, XAS and XRD methods are sample-averaging techniques, and their sensitivity to the processes on the NPs surface is limited. To obtain surface-specific information on the Ni_3Ga_1 and Ni_5Ga_3 NP catalysts during H_2 activation and the CO_2 hydrogenation reaction, complementary NAP-XPS measurements were performed, in which Ni 2p, Ga 2p, C 1s and O 1s spectra were acquired for all conditions probed. The use of two different photon energies, resulting in inelastic mean free paths between 0.6-1.2 nm for the Ga 2p spectra and in 0.8-1.1 nm for the Ni 2p spectra, facilitated to some extent a depth-profiling of the NP structure and chemical state. Nonetheless, considering that the NP sizes (AFM height) were on the order of 1.4 nm (Ni_5Ga_3 sample) and 1.5 nm (Ni_3Ga_1 sample), see **Figure 1**, even the low photon energy (1250 eV) probed a large fraction of the NP volume, yet, the overall probability that the signals stem from the NP surface is higher compared to when using 1540 eV as photo energy. As described in Section 3.1, the samples used for the NAP-XPS measurements consisted of NPs dip-coated onto planar SiO_2/Si(100) supports, see **Figure 1(a-c)**). To remove carbon contamination, the NP samples were first exposed to 0.7 mbar of O_2 at a temperature of 400°C. Thereafter, they were reduced in H_2 and measured at 500°C and then at 700°C, in line with the activation temperatures used in our XRD and catalytic activity studies, respectively. A total pressure of 1.1 mbar (2.1 mbar) was used for the Ni_3Ga_1 (Ni_5Ga_3) nanocatalysts. The subsequent CO_2 hydrogenation study was carried out at three different temperatures (180°C, 210°C, and 240°C). An H_2:CO_2 3:1 mixture was used with a total pressure of 1.7 mbar (2.1 mbar) for the Ni_3Ga_1 (Ni_5Ga_3) NP samples. Finally, additional spectra were acquired for both samples during the subsequent exposure to pure H_2 and pure CO_2, employing again a pressure of 1.7 mbar (2.1 mbar) for the Ni_3Ga_1 (Ni_5Ga_3) NP sample. For the investigation of the Ni_3Ga_1 sample, slightly lower pressures had to be used not to damage the electron analyzer by a too high pressure in the 3rd differentially pumped stage. Yet, we consider the NAP-XPS results deduced on the individual samples as comparable.

Figure 9(a,b) shows selected Ga 2p and Ni 2p spectra from the measurement sequence for the Ni_3Ga_1 NP sample. The corresponding spectra for the Ni_5Ga_3 sample are shown in **Figure S16** in the Supporting Information. The oxidized fractions of the metallic Ni and Ga, as deduced from the fits to the XPS spectra, are displayed in **Figure 10(a,b)** for the Ni_3Ga_1 and the Ni_5Ga_3 NPs, respectively. These XPS data were obtained from the deduced peak areas that were corrected for

the relative sensitivity factors and are accordingly representative of the amount of the corresponding material in the sample. The relative sensitivity factors are determined by the photoionization cross sections [40-42] and the inelastic mean free path of the outgoing electrons [33], where the particle elemental composition and the kinetic energy of the electron after photoionization were taken into account. We find the general trends in oxidation state under the different environments for both samples similar, yet, there are subtle differences as discussed below.

During the O_2 treatment, both samples are completely oxidized. Upon activation in H_2, the Ni species in both samples become completely reduced at 500°C (in line with our XRD and XAS measurements), while the reduction of the Ga_2O_3 species lags behind, which is also in agreement with our XAS results. As can also be deduced from the spectra in **Figure 10(a)**, even under reducing conditions at 700°C, there is still a clear Ga oxide peak visible, implying that even under these conditions Ga is not yet fully reduced and Ga_2O_3 is still present on the NP surface. According to the quantitative analysis summarized in **Figure 11(a,b)**, the final oxidized fraction as obtained with a photon energy of 1540 eV is higher for the Ni_5Ga_3 NPs and amounts to 40%, whereas in the Ni_3Ga_1 NPs the fraction of oxidized species amounts to only 27%. This finding is in agreement with our bulk-sensitive XAS results, which also revealed a tendency of the gallium species to be more easily reduced for the Ni_3Ga_1 composition. Note, however, that the pressure gap compared to our *operando* XAS measurements may inhibit the reduction of surface Ga_2O_3 in our NAP XPS measurements. Moreover, in line with prior literature [16], our XPS data show that the formation of Ga_2O_3 occurs on the nanoparticle surface, for which our bulk-averaging XAS measurements are less sensitive.
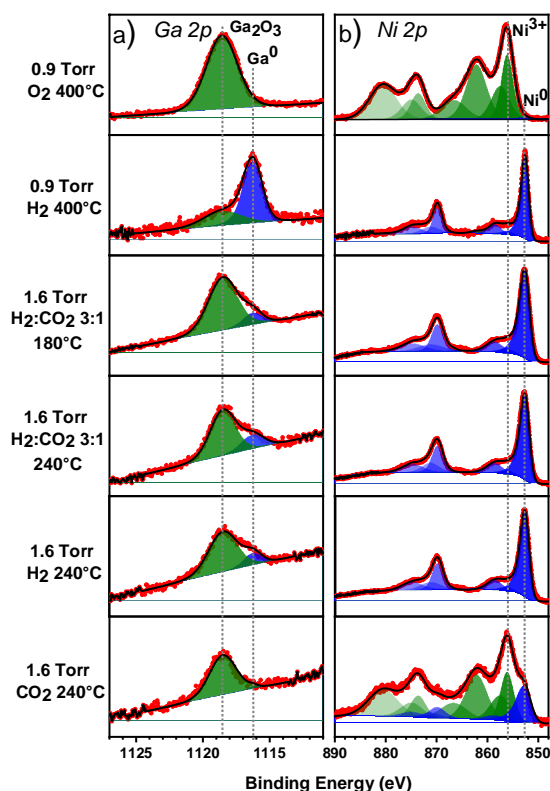
Figure 9: *NAP-XPS spectra of (a) Ga 2p$_{3/2}$ and (b) Ni 2p$_{3/2}$ recorded for the Ni$_3$Ga$_1$ sample under the different gaseous environments using 1540 eV photon energy. The XPS data fits are also shown, with partial contributions from elemental Ga and Ni given in blue, and the contributions from Ga$_2$O$_3$ and NiO-like species shown in green.*

It is striking that, as can be directly deduced from **Figure 9** and **Figure 10(a)**, an almost complete oxidation of the surface Ga occurs for the Ni$_3$Ga$_1$ NPs under reaction conditions, while Ni is found to remain metallic regardless of the reaction temperature. Experiments using the more surface-sensitive photon energy of 1250 eV revealed the oxidized Ga fraction to be close to 100% under reaction conditions, while a slightly lower oxide fraction was observed with the 1540 eV photon energy. The depth profiling thus suggests that the completely oxidized Ga is located on the surface of the Ni$_3$Ga$_1$ NPs, in line with earlier studies [6]. The high segregation of Ga$_2$O$_3$ is explained by the fact that Ga features a higher affinity for oxygen and is accordingly pulled to the NP surface upon oxide formation [6]. The lack of a significant oxidized Ga contribution in our *operando* XAS data collected for the Ni$_3$Ga$_1$ sample under reaction conditions thus can be

explained by the fact that Ga oxidation is limited to the surface of the NPs, and the insufficient sensitivity of the XAS method to the surface composition masks this contribution. As can be deduced from **Figure 10(a)**, this chemical composition of the Ni_3Ga_1 sample is maintained under reaction conditions, independent of the reaction temperature probed.
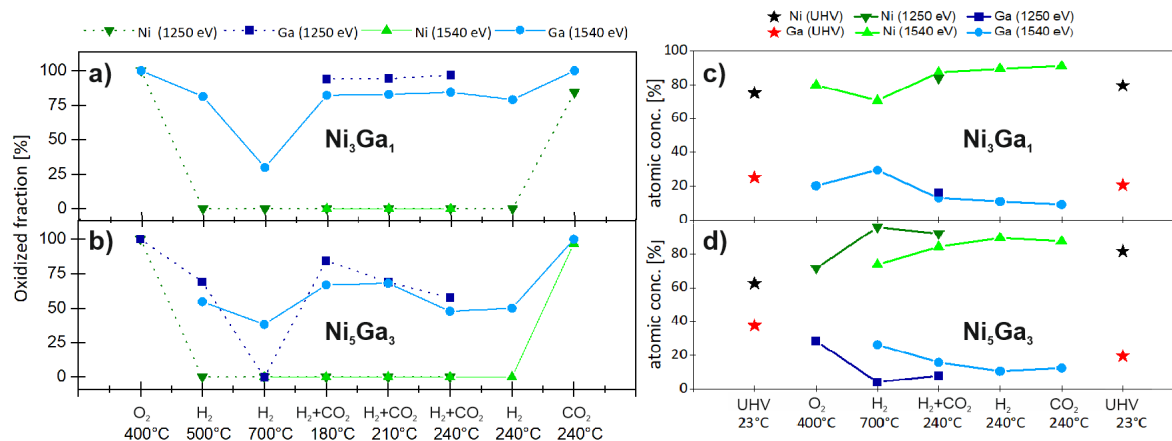

Figure 10: *Oxidized fractions of Ni and Ga under the different gaseous environments indicated on the graph plotted for two photon energies (1250 and 1540 eV). Results for the (a) Ni_3Ga_1 and the (b) Ni_5Ga_3 samples are shown. Relative atomic fractions of Ni and Ga under different gaseous environments and for two photon energies (1250 and 1540 eV) are displayed in (c) for the Ni_3Ga sample and in (d) for the Ni_5Ga_3 sample. The stars at the beginning of the series correspond to the nominal concentrations obtained in UHV before reaction, while those at the end of the series correspond to measurements performed in UHV after the reaction series, which was carried out at a total pressures of 1.7 mbar (2.1 mbar) for the Ni_3Ga_1 (Ni_5Ga_3) NPs.*

For the Ni_5Ga_3 NPs the quantitative NAP-XPS analysis suggests that the oxidized fraction of Ga is smaller compared to the Ni_3Ga_1 sample, around 75% at 180°C. Moreover, the amount of Ga_2O_3 depends on the reaction temperature for the Ni_5Ga_3 NPs, and decreases with increasing temperature. Thus, at 240°C the oxidized fraction of Ga has decreased to around 50%. This temperature-dependence of the Ga oxidation degree in the Ni_5Ga_3 NPs, in the temperature range where the catalyst has been found in previous studies most active toward methanol production [6,7,10], may be essential for optimizing the catalyst performance. During the subsequent exposure of the NiGa NPs to pure H_2, succeeding the probed reaction conditions, the oxidation state of the

NPs remains unchanged, regardless of the particle composition, as can be seen in **Figure 10(a,b)**. The exposure to pure CO_2 thereafter resulted for both particle compositions in the complete oxidation of Ga and in the partial oxidation of Ni.

The quantitative NAP-XPS analysis, moreover, allowed us to deduce the Ni and Ga metal atomic concentrations. The results for the Ni_3Ga_1 and the Ni_5Ga_3 NPs are plotted in **Figure 10(c,d)**, and as a function of the different probed conditions. In line with the results shown in **Figure 10(a,b)**, the data reveal that the metallic Ni/Ga ratio exceeds the nominal concentration under reaction conditions, which can be partially ascribed to the formation of Ga_2O_3. The absence of metallic Ga on the NP surface under reaction conditions, which can be deduced from the data measured with a photon energy of 1250 eV, is moreover in line with the existence of a Ga_2O_3-rich nanoparticle shell. It is interesting to note that the experimental Ni/Ga ratio is lower as compared to the nominal one for the H_2 reduction conditions at 500°C. This implies that Ga is reduced at an earlier stage than Ni, which is in line with our XAS results. Finally, for both NiGa compositions, the data reveal that a chemical restructuring occurs under reducing conditions, with the Ni atoms segregating to the particle surface resulting in a Ni-rich shell and a Ga-rich core, a tendency that appears to be maintained under CO_2 hydrogenation reaction conditions. This can be inferred from the relative atomic fractions displayed in **Figure 10(c,d).** They show that under H_2 activation and reaction conditions, the relative atomic fraction of metallic Ni increased with respect to the as-prepared state, especially for the NP shell probed with the lower photon energy of 1250 eV.

Note, that although the differences in average oxidation state and chemical composition observed for the two samples are not large, they can have a drastic impact on the catalytic performance. In this respect, we want to highlight that for many catalytic processes the active sites are composed of only a few atoms or minority species [21,43,44], especially when NP catalysts are employed.

3.3.2 Catalytic performance

Prior to the activity tests, the samples underwent the same activation procedure used in our *in-situ* XRD study (1 bar H_2 at 700°C for 7.5 h). Thereafter, the samples were cooled down to 160°C in H_2 flow, followed by the introduction of the reaction gas mixture and the probing of the catalyst activity as a function of the reaction temperature.
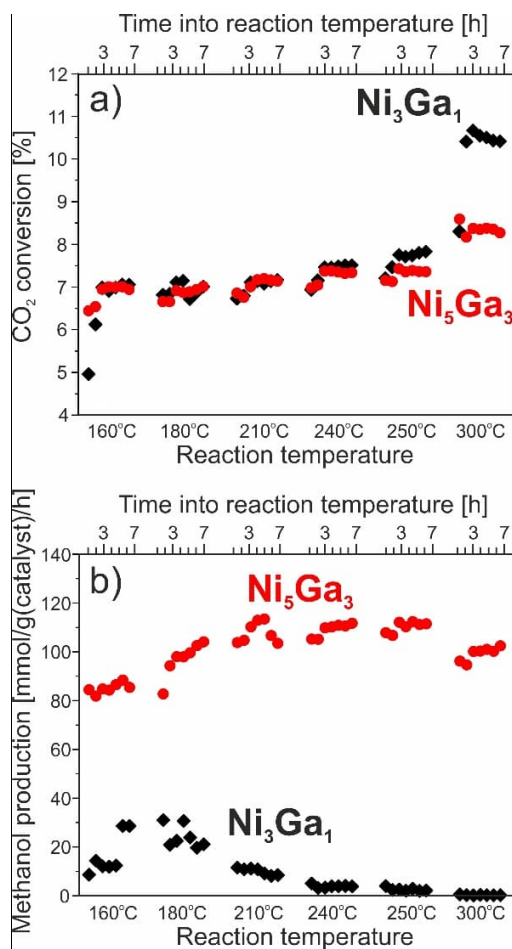

Figure 11: *CO_2 conversion (a) and methanol production (b) for the Ni_3Ga_1 and the Ni_5Ga_1 samples as a function of the reaction temperature and time during CO_2 hydrogenation at 1 bar.*

Figure 11(a) displays the CO_2 conversion and the methanol production for the Ni_3Ga_1 and the Ni_5Ga_3 NPs, respectively, for the different probed temperatures (160°C, 180°C, 210°C, 240°C,

250°C, and 300°C). The conversion of CO_2 increases for both samples as a function of the sample temperature. While at lower temperatures the CO_2 conversion is comparable for both samples, it is at 300°C for the Ni_3Ga_1 NPs about 1.5 times higher compared to the one of the Ni_5Ga_3 NPs. Nonetheless, the methanol selectivity of the Ni_3Ga_1 sample is about one order of magnitude lower. Although Ga_2O_3 has been concluded to be a good promoter for the synthesis of methanol [6], we ascribe here the high methanol production of the Ni_5Ga_3 catalyst to the presence of the δ-Ni_5Ga_3 phase. This is because Ga_2O_3 was present on the surface of both samples under reaction conditions and therefore, it cannot be held responsible for the clear discrepancies observed in methanol production of both samples. While for the Ni_3Ga_1 NPs the selectivity toward methanol decreases with increasing temperature, the methanol production becomes maximum for the Ni_5Ga_3 catalyst in the range of 210-240°C, see **Figure 11(b)**, which is in agreement with previous reactivity results reported for non-micelle-based Ni_5Ga_3 NP powder catalysts [6,7,10].
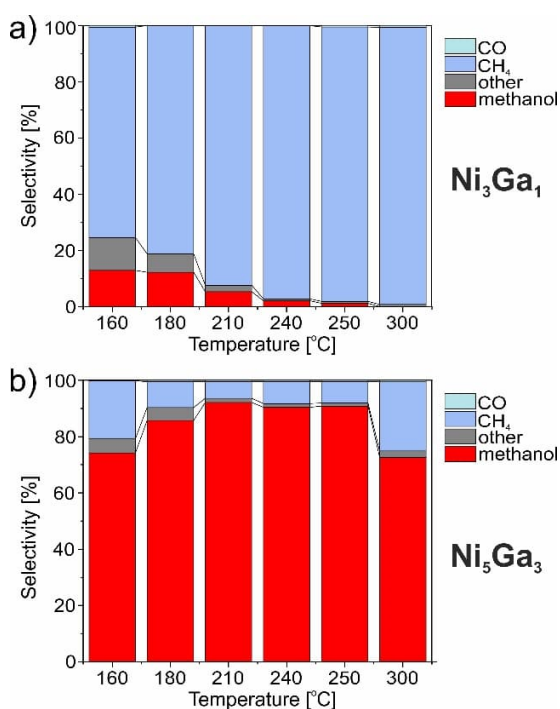

Figure 12: *Product selectivities for the (a) Ni_3Ga_1 and (b) Ni_5Ga_3 samples as a function of the reaction temperature during CO_2 hydrogenation at 1 bar. For both samples "other" refers to ethanol, C_3H_6, C_3H_8, C_2H_6, and C_5H_{12}. The product selectivities correspond to the mean values from the data of five hourly gas chromatography injections (starting 3 h into the set temperature, see **Figure 11**).*

Information on the respective reaction products as a function of temperature obtained from the analysis of gas chromatography data for the two NiGa samples is summarized in **Figure 12(a,b)**. These data show that the selectivity of the Ni_5Ga_3 sample for methanol production increases from 86% at 180°C to 92% at 210°C, **Figure 12(b)**. At higher temperatures the methanol production is found to decrease again. However, this change is more gradual, resulting in a methanol selectivity of still 90% at 240°C. The Ni_5Ga_3 catalyst shows also a high selectivity for the production of CH_4, but only for temperatures well below or above 210°C (21% at 160°C and 25% at 300°C).

Figure 12(a) reveals that the Ni_3Ga_1 sample displays a completely different product distribution. Thus, the methane yields are found to be extremely high, as is the case for methanation catalysts like Ni [7,45,46], which indicates that there could be excess metallic Ni present on the Ni_3Ga_1 NP surface. The methane production was concluded to increase as a function of the sample temperature (75% at 160°C up to 99% at 300°C). The highest methanol selectivity achieved with the Ni_3Ga_1 sample is observed at 160°C and constitutes less than 13%, which is dramatically lower compared to the highest methanol selectivity of 92% of the Ni_5Ga_3 NP catalyst observed at 210°C. Note also the low selectivity toward undesired CO production of less than 1% for both NP samples and at all temperatures, which clearly distinguishes the NiGa catalyst from the CuZn system at ambient pressures [7,10]. It should be however noted that there is almost no change in CO_2 conversion in the temperature range between 160 and 250°C. In this temperature range, the yields of the two main products, methanol and methane, is relatively stable for both samples, which results in a stable CO_2 conversion. On the other hand, only for temperatures higher than 250°C a steep increase in the methane production is observed. This is in line with findings in the literature for Ni catalysts, e.g. [45], and is most clearly seen for our Ni_3Ga_1 catalyst, which features a high amount of metallic Ni. Accordingly, the CO_2 conversion features a significant increase at 300°C, in particular for the Ni_3Ga_1 sample, since more metallic Ni is present and favors methane formation.

4 Discussion

In this work we used complementary *in situ* and *ex situ* techniques to shed light on the structural, chemical and compositional evolution of micelle Ni_3Ga_1 and Ni_5Ga_3 NPs during H_2 activation and CO_2 hydrogenation at various temperatures. The multiprobe approach allowed us to

deduce the correlation between the catalyst surface and bulk structure, the chemical composition and the reaction products, including the methanol yield. Based on these findings we infer the scenario, schematically depicted in **Figure 13**.

Initially, prior to the H_2 activation, the Ni_5Ga_3 and the Ni_3Ga_1 samples are fully oxidized into NiO crystallites (as evidenced by XRD, XAS, and XPS) and into amorphous and highly dispersed Ga_2O_3 (XAS, XPS). Due to the more negative standard enthalpy of formation, the Ga_2O_3 is located at the crystallite surface [16] (as evidenced by XPS). During the initial H_2 activation steps at low temperatures (100-200°C), Ga_2O_3 starts to be reduced for both samples prior to NiO, however, at higher temperatures the reduction rate of Ni exceeds that of the Ga species (XAS). The reduction temperature for NiO into metallic Ni crystallites is found to be slightly dependent on the particle composition (XRD, XAS). For the Ni_3Ga_1 sample, metallic Ni coexists with NiO already at 300°C (XRD), and clearly dominates the sample composition at 400°C. For the Ni_5Ga_3 sample, metallic Ni is first observed at 350-400°C (XRD, XAS). At 400°C the Ni_5Ga_3 sample is completely reduced into the intermediate metallic Ni phase. This reduction step is also associated with a fragmentation of the NPs (XRD) for both samples. Upon the reduction at higher temperatures (500°C and higher), Ga is progressively being incorporated into the metallic Ni. As a result, at 700°C under H_2, the Ni_3Ga_1 sample consists of the α'-Ni_3Ga_1 phase only, while the Ni_5Ga_3 sample shows a coexistence of the α'-Ni_3Ga_1 and the δ-Ni_5Ga_3 phase (XRD, XAS), as well as of remaining oxidized Ga (XPS, XAS). In addition, the XPS data suggest the presence of metallic Ni on the surface of both NP samples. The coexistence of the two NiGa alloys for the Ni_5Ga_3 sample even under such high activation temperatures can be traced back to the fact that both, metallic Ni and α'-Ni_3Ga_1, feature fcc structures, whereas the δ-Ni_5Ga_3 phase is characterized by an orthorhombic lattice. As a consequence, the restructuring into the δ-Ni_5Ga_3 phase appears to be energetically less favorable. The coexistence of the δ-Ni_5Ga_3 and the α'-Ni_3Ga_1 phases, the latter featuring a lower percentage of Ga, implies the presence of excess Ga for the reduced Ni_5Ga_3 sample, which explains the presence of oxidized Ga species even after the H_2 activation for this sample (XAS).

Under CO_2 hydrogenation reaction conditions, the Ga in both samples oxidizes again, leaving the particles with a Ga_2O_3-rich shell (XPS). Our data indicates that the oxidation of the Ga species is more pronounced for the Ni_3Ga_1 sample, which, in turn, implies that this alloy composition also

features a higher amount of excess metallic Ni as compared to the Ni_5Ga_3 sample. This can also be concluded from our *operando* XRD data measured on the sample during CO_2 hydrogenation. In particular, the relatively high amount of metallic Ni in the Ni_3Ga_1 sample (ranging from 43% at 300°C to 67% at 180°C), deduced from the Rietveld analysis of the corresponding *operando* XRD scans measured under working conditions, see **Figure S4** and **Table S5** in the Supporting Information, may explain the high production of methane, since Ni acts as a methanation catalyst [7,45,46]. While for the Ni_3Ga_1 sample the amount of Ga_2O_3 and thus of metallic Ni in the NP shell remains more or less constant, even when increasing the reaction temperature (XPS), higher temperatures may result in the reduction of Ga_2O_3 for the Ni_5Ga_3 sample. In turn, for the Ni_5Ga_3 sample, more NiGa alloy phases form, mainly the α'-Ni_3Ga_1 phase (XRD), which brings along a decrease in the excess of metallic Ni. This could explain why the Ni_3Ga_1 sample shows an unchanged high selectivity toward the production of methane, even at elevated temperatures, while the Ni_5Ga_3 sample is active toward the production of methane at lower reaction temperatures up to 180°C when a high amount of Ga_2O_3 is present in the NP shell and thus, excess metallic Ni is available. Note in this respect, that the oxidation of Ga to Ga_2O_3 concomitantly results in the depletion of Ga from the metallic NiGa phase. With α'-Ni_3Ga_1 being the NiGa phase with the highest Ni content, depletion of Ga from the Ni_3Ga_1 sample leads to the coexistence of α'-Ni_3Ga_1 and metallic Ni, as evidenced in our operando XRD results, see **Figure S4** and **S5**, and **Tables S5** and **S6** in the Supporting Information. On the other hand, our XRD data showed that the depletion of Ga on the Ni_5Ga_3 sample resulted in the formation of the α'-Ni_3Ga_1 phase and its coexistence with the δ-Ni_5Ga_3 phase. With the Ni_3Ga_1 sample being even more oxidized than the Ni_5Ga_3 sample (XPS), a higher amount of metallic Ni was observed (XRD).

For temperatures of 210°C and higher, the selectivity of the Ni_5Ga_3 sample switches in favor of methanol production, which can be explained by the presence of the δ-Ni_5Ga_3 phase, but also by the absence of excess metallic Ni that favors the production of methane. Accordingly, we find that excess metallic Ni, the amount of which is reversely proportional to the amount of Ga_2O_3, could play a decisive role in the selectivity of the NiGa systems, as it may inhibit the production of methanol. Similar observations, namely that the alloyed phase of intermetallic compounds, and not the presence of their respective elements, provides highly selective hydrogenation catalysts

[47-49], also toward methanol production, has earlier been reported for the Pd-Ga system, and was ascribed to the resulting modification of the electronic states in the intermetallic compound alloy. Based on our results, we conclude that it is the presence of the δ-Ni$_5$Ga$_3$ phase in the Ni$_5$Ga$_3$ NPs the one responsible for their high methanol production. Furthermore, with Ga$_2$O$_3$ present in both samples, we consider that it cannot be solely responsible for the high methanol output displayed by the Ni$_5$Ga$_3$ sample. On the other hand, the metallic Ni phase present in the Ni$_3$Ga$_1$ NPs under reaction conditions is considered responsible for their high methane production. The insights from our in situ and operando spectroscopic characterization thus allows us to directly identify the species responsible for the drastically different catalytic properties observed for Ni$_5$Ga$_3$ and Ni$_3$Ga$_1$ NPs.
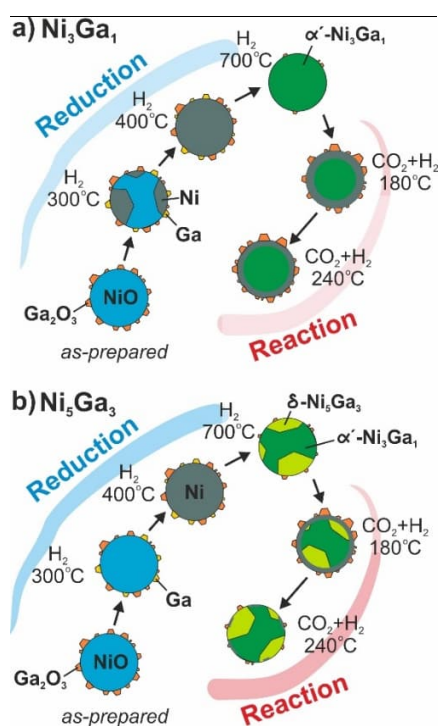

Figure 13: *Cartoon illustrating the evolution of the structure and chemical composition of the (a) Ni$_3$Ga$_1$ and the (b) Ni$_5$Ga$_3$ samples upon activation in H$_2$ and under CO$_2$ hydrogenation conditions at several temperatures as deduced from a multi-technique approach employed in this work. The color-coding is as follows: orange:, Ga$_2$O$_3$, blue, NiO; yellow, Ga; grey, Ni; dark green, α'-Ni$_3$Ga$_1$; light green, δ-Ni$_5$Ga$_3$.*

5 Conclusions

In the present work, we unraveled the structural and compositional changes of micelle-based Ni_3Ga_1 and Ni_5Ga_3 NP samples under H_2 activation and CO_2 hydrogenation conditions at ambient pressures using a multiprobe approach. We concluded for both samples that under activation in H_2 at 1 bar, the initially oxidized NPs undergo a reduction into an intermediate metallic Ni phase, with Ga being progressively incorporated at temperatures higher than 500°C to form NiGa alloys. Regardless of the particle composition, Ni was found to become reduced at higher temperatures compared to Ga, yet with a higher rate. Moreover, the Ni in Ni_3Ga_1 is reduced already at a slightly lower temperature (300°C) as compared to the Ni in Ni_5Ga_3 (400°C). The activation in H_2 results in the formation of the α'-Ni_3Ga_1 phase for the Ni_3Ga_1 sample. For the reduced Ni_5Ga_3 sample, the coexistence of α'-Ni_3Ga_1 and δ-Ni_5Ga_3 metallic phases, with a respective ratio of 60% to 40%, and of Ga_2O_3 phases was concluded. In this respect, our *in situ* spectroscopy and diffraction data revealed that for the activation of the NiGa pre-catalysts temperatures of at least 500°C are needed to achieve the stabilization of the δ-Ni_5Ga_3 phase. We found the micelle-based NP samples to be catalytically active for methanol synthesis under CO_2 hydrogenation conditions at ambient pressure, with the Ni_5Ga_3 sample featuring a much higher methanol yield (by about one order of magnitude) compared to the Ni_3Ga_1 sample. This can be traced back to the presence of the δ-Ni_5Ga_3 phase in the Ni_5Ga_3 samples, but also to the lower amount of Ga_2O_3 and metallic Ni in the nanoparticle shell compared to the Ni_3Ga_1 NPs, which are under reaction conditions oxidized to a greater extent, with the Ga_2O_3 stable independent of the sample temperature. We conclude that the metallic Ni in the Ni_3Ga_1 NPs inhibits a high methanol yield as it promotes the production of methane.

The present work, moreover, underlines the utmost importance of the combination of various complementary *in situ* and *operando* techniques for the investigation of size-controlled NP model catalyst systems, as it allows one to correlate the structural and chemical catalytic properties to the catalytic performance, which is essential for further catalyst optimization. The resulting detailed overview over the structural and electronic characteristics of NiGa NP catalysts can serve as a basis for future theoretical calculations.

Acknowledgements

References

[1] G. A. Olah, A. Goeppert, and G. K. Surya Prakash, Beyond oil and gas: the methanol economy (Wiley-VHC, Weinheim, Germany, 2011).

[2] A. M. Appel et al., Frontiers, opportunities and challenges in biochemical and chemical catalysis of CO_2 fixation, Chem. Rev. 113, 6621 (2013).

[3] S. Kattel et al., Active sites for CO_2 hydrogenation to methanol on Cu/ZnO catalysts, Science 355, 1296 (2017).

[4] K. Klier, Methanol synthesis, Advances in Catalysis 31, 243 (1982).

[5] M. Bukhtiyarova, T. Lunkenbein, K. Kähler, and R. Schlögl, Methanol synthesis from industrial CO_2 sources: a contribution to chemical energy conversion, Catal. Letters 147, 416 (2017).

[6] A. Gallo, J. L. Snider, D. Sokaras, D. Nordlund, T. Kroll, H. Ogasawara, L. Kovarik, M. S. Duyar, and T. F. Jaramillo, Ni_5Ga_3 catalysts for CO_2 reduction to methanol: exploring the role of Ga surface oxidation/reduction on catalytic activity, Appl. Catal. B: Environm. 267, 118369 (2020).

[7] F. Studt, I. Sharafutdinov, F. Abild-Pedersen, C. F. Alkjaer, J. S. Hummelshoj, S. Dahl, I. Chorkendorff, and J. K. Norskov, Discovery of a NiGa catalyst for carbon dioxide reduction to methanol, Nature Chem. 6, 320 (2014).

[8] M. Armbrüster, Intermetallic compounds in catalysis – a versatile class of materials meets interesting challenges, Science and Technology of Advanced Materials 21, 303 (2020).

[9] T. E. L. Smitshuysen, M. R. Nielsen, T. Pruessmann, A. Zimina, T. L. Sheppard, J.-D. Grunwaldt, I. Chorkendorff, and C. D. Damsgaard, Optimizing Ni-Fe-Ga alloys into Ni_2FeGa for the hydrogenation of CO_2 into methanol, ChemCatChem 12, 3265 (2020).

[10] I. Sharafutdinov, C. F. Elkjaer, H. W. P. de Carvalho, D. Gardini, G. L. Chiarello, C. D. Damsgaard, J. B. Wagner, J.-D. Grunwaldt, S. Dahl, and I. Chorkendorff, Intermetallic compounds of Ni and Ga as catalysts for the synthesis of methanol, J. Catal. 320, 77 (2014).

[11] C. L. Chiang, K. S. Lin, and Y. G. Lin, Preparation and Characterization of Ni_5Ga_3 for methanol formation vie CO_2 hydrogenation, Top. Catal. 60, 685 (2017).

[12] P. Gao, L. Zhang, S. Li, Z. Zhou and Y. Sun, Novel heterogeneous catalysts for CO_2 hydrogenation to liquid fuels, ACS Cent. Sci. 6, 1657 (2020).

[13] X. Jiang, X. Nie, X. Guo, C. Song, and J. G. Chen, Recent advances in carbon dioxide hydrogenation to methanol via heterogeneous catalysis, Chem. Rev. 120, 7984 (2020).

[14] J. Zhong, X. Yang, Z. Wu, B. Liang, Y. Huang, and T. Zhang, State of the art and perspectives in heterogeneous catalysis of CO_2 hydrogenation to methanol, Chem. Soc. Rev. 49, 1385 (2020).

[15] M. M-J. Li, and S. C. E. Tsang, Bimetallic catalysts for green methanol production via CO_2 and renewable hydrogen: a mini-review and prospects, Catal. Sci. Technol. 8, 3450 (2018).

[16] M. Wencka, J. Kovac, V. D. B. C. Dasireddy, B. Likozar, A. Jelen, S. Vrtnik, P. Gille, H. J. Kim, and J. Dolinsek, The effect of surface oxidation on the catalytic properties of Ga_3Ni_2 intermetallic compound for carbon dioxide reduction, Journal of Analytical Science and Technology 9, 1 (2018).

[17] H. Okamoto, Ga-Ni (Gallium-Nickel), Journal of Phase Equilibria and Diffusion 31, 557 (2010).

[18] W. Jochum, S. Penner, R. Kramer, K. Föttinger, G. Rupprechter, B. Klötzer, Defect formation and the water-gas shift reaction on β-Ga_2O_3, Journal of Catalysis 256, 278 (2008).

[19] Y.-X. Pan, Z.-Q. Sun, H.-P. Cong, Y.-L. Men, S. Xin, J. Song, S.-H. Yu, Photocatalytic CO_2 reduction highly enhanced by oxygen vacancies on Pt-nanoparticle-dispersed gallium oxide, Nano Research 9, 1689 (2016).

[20] F. Behafarid, and B. Roldan Cuenya, Nanoepitaxy using micellar nanoparticles, Nano Lett. 11, 5290 (2011).

[21] B. Roldan Cuenya, Synthesis and catalytic properties of metal nanoparticles: size, shape, support, composition, and oxidation state effects, Thin Solid Films 518, 3127 (2010).

[22] A. Bergmann, and B. Roldan Cuenya, Operando insights into nanoparticle transformations during catalysis, ACS Catalysis 9, 10020 (2019).

[23] B. Roldan Cuenya, and F. Behafarid, Nanocatalysis: size- and shape-dependent chemisorption and catalytic reactivity, Surface Science Reports 70. 135 (2015).

 [24] A. A. Coelho, TOPAS and TOPAS-Academic: an optimization program integrating computer algebra and crystallographic objects written in C++, J. Appl. Cryst. 51, 210 (2018).

[25] L. Simonelli, C. Marini, W. Olszewski, M. Avila Perez, N. Ramanan, G. Guilera, V. Cuartero, and K. Klenentiev, CLAESS: The hard x-ray absorption beamline of the ALBA CELLS synchrotron, Cogent Physics 3, 1231987 (2016).

[26] B. Ravel and M. Newville, ATHENA, ARTEMIS, HEPHAESTUS: data analysis for X-ray absorption spectroscopy using IFEFFIT, J. Synchrotron Rad. 12, 537 (2005).

[27] J. Timoshenko, H. S. Jeon, I. Sinev, F. T. Haase, A. Herzog, and B. Roldan Cuenya, Linking the evolution of catalytic properties and structural changes in copper-zinc nanocatalysts using operando EXAFS and neural-networks, Chem. Sci. 11, 3727 (2020).

[28] J. Timoshenko, A. Anspoks, A. Cintins, A. Kuzmin, J. Purans, and A. I. Frenkel, Neural network approach for characterizing structural transformations by X-ray absorption fine structure spectroscopy, Phys. Rev. Lett. 120, 225502 (2018).

[29] J. Timoshenko, and A. I. Frenkel, "Inverting" X-ray absorption spectra of catalysts by machine learning in search for activity descriptors, ACS Catal. 9, 10192 (2019).

[30] J. Timoshenko, and A. I. Frenkel, Probing structural relaxation in nanosized catalysts by combining EXAFS and reverse Monte Carlo methods, Catal. Today 280, 274 (2017).

[31] J. Timoshenko, Z. Duan, G. Henkelman, R. M. Crooks, and A. I. Frenkel, Solving the structure and dynamics of metal nanoparticles by combining X-ray absorption fine structure spectroscopy and atomistic structure simulations, Annu. Rev. Anal. Chem. 12, 501 (2019).

[32] J. Timoshenko, M. Ahmadi, and B. Roldan Cuenya, Is there a negative thermal expansion in supported metal nanoparticles? An in situ X-ray absorption study coupled with neural network analysis, J. Phys. Chem. C 123, 20594 (2019).

[33] S. Tanuma, C.J. Powell, D. R, Penn, Calculations of electron inelastic mean free paths, Surface and Interface Analysis 21, 165 (1993).

[34] N. Fairly, V. Fernandez, M. Richard-Plouet, C. Guillot-Deudon, J. Walton, E. Smith, D. Flahaut, M. Greiner, M. Biesinger, S. Tougaard, D. Morgan, J. Baltrusaitis, Systematic and collaborative approach to problem solving using X-ray photoelectron spectroscopy, Appl. Surf. Sci. Adv. 5, 100112 (2021).

[35] P. Klapetek, D. Necas, and C. Anderson, Gwyddion – free SPM data analysis software (http://gwyddion.net)

[36] Persson Kristin, Materials data on Ni= by Materials Project, United States, 10.17188/1193796.

[37] Persson Kristin, Materials data on Ni by Materials Project, United States, 10.17188/1199153.

[38] Persson Kristin, Materials data on $GaNi_3$ by Materials Project, United States, 10.17188/1307937.

[39] Persson Kristin, Materials data on Ga_3Ni_5 by Materials Project, United States, 10.17188/1187799.

[40] M. B. Trzhaskovskaya, V. I. Nefedov, V. G. Yarzhemsky, Photoelectron angular distribution parameters for elements Z=1 to Z=54 in the photoelectron energy range 100-5000 eV, Atomic data and Nuclear data tables 77, 97 (2001).

[41] M. B. Trzhaskovskaya, V. I. Nefedov, V. G. Yarzhemsky, Photoelectron angular distribution parameters for elements Z=55 to Z=100 in the photoelectron energy range 100-5000 eV, Atomic data and Nuclear data tables 82, 257 (2002).

[42] J. J. Yeh, I. Lindau, Atomic subshell photoionization cross sections and asymmetry parameters: 1≤Z≤103, Atomic data and nuclear tables 32, 1 (1985).

[43] B. Ni, and X. Wang, Face the Edges: Catalytic active sites of nanomaterials, Adv. Sci. 2, 1500085 (2015).

[44] S. Mitchell, and J. Perez-Ramirez, Single atom catalysis: a decade of stunning progress and the promise for a bright future, Nature Commun. 11, 4302 (2020).

[45] T. A. Le, J. K. Kang, E. D. Park, CO and CO_2 methanation over Ni/SiC and Ni/SiO2 catalysts, Topics in Catalysis 61, 1537 (2018).

[46] N. M. Martin, F. Hemmingson, A. Schaefer, M. Ek, L. R. Merte, U. Hejral, J. Gustafson, M. Skoglundh, A.-C. Dippel, O. Gutowski, M. Bauer, and P.-A. Carlsson, Structure-function relationship for CO_2 methanation over ceria supported Rh and Ni catalysts under atmospheric pressure conditions, Catal. Sci. Technol. 9, 1644 (2019).

[47] K. Kovnir, M. Armbrüster, D. Teschner, T. V. Venkow, L. Szentmiklosi, F. C. Jentoft, a. Kmop-Gericken, and R. Schlögl, In situ surface characterization of the intermetallic compound PdGa – a highly selective hyrdrogenation catalyst, Surf. Scie. 603, 1784 (2009).

[48] M. Armbrüster, K. Kovnir, M. Behrens, D. Teschner, Y. Grin, and R. Schlögl, Pd-Ga intermetallic compounds as highly selective semihydrogenation catalysts, J. Am. Chem. Soc. 132, 14745 (2010).

[49] R. Manrique, J. Rodriguez-Pereira, S. A. Rincon-Ortiz, J. J. Bravo-Suarez, V. G. Baldovino-Medrano, R. Jimenez, and A. Karelovic, The nature of the active sites of Pd-Ga catalysts in the hydrogenation of CO_2 to methanol, Catalysis Science & Technology 10, 6644 (2020).